Design of a 10 MeV, 1000 kW average power electron-beam accelerator for wastewater treatment applications

R. C. Dhuley,* I. Gonin, S. Kazakov, T. Khabiboulline, A. Sukhanov, V. Yakovlev, A. Saini, N. Solyak, A. Sauers, and J. C. T. Thangaraj
Fermi National Accelerator Laboratory, Batavia, Illinois 60510, USA

K. Zeller and B. Coriton
General Atomics, San Diego, California 92186, USA

R. Kostin
Euclid Techlabs, LLC, Bolingbrook, Illinois 60440, USA

(Received 21 December 2021; accepted 1 April 2022; published 21 April 2022)

We present the technical and engineering design of a medium energy (10 MeV) and high average power (1000 kW) electron-beam accelerator intended for irradiation treatment of high-volume industrial and municipal wastewater. The accelerator uses a Nb_3Sn superconducting radio-frequency (SRF) cavity for producing the high average beam power with >90% rf to beam efficiency. The design of the accelerator is tailored for industrial settings by adopting the cryocooler conduction-cooling technique for the SRF cavity instead of a conventional liquid helium bath cryosystem. The technical design is supplemented with a detailed analysis of capital and operating cost of the accelerator. The designed accelerator can treat up to 12 million gallons per day of wastewater, requires capital of ∼$8 M for construction, and has ∼13.5 ¢/ton/kGy in material processing cost.

DOI: 10.1103/PhysRevAccelBeams.25.041601

I. INTRODUCTION

Energetic electron beams (*e*-beams) are a powerful tool for numerous applications ranging from scientific R&D to industrial processes. *E*-beams with GeV energy are used to probe matter for particle physics research and generate powerful x rays for photon science research [1]. MeV-scale (1 to tens of MeV) *e*-beams are a material processing tool for altering the physical, chemical, molecular, and biological properties of materials. These include polymerization, medical and food sterilization, environmental remediation, wastewater treatment, sludge and biosolids treatment, etc., [2]. X rays generated using MeV-scale *e*-beams find application in cargo scanning and production of terahertz light for security imaging applications [3]. More recently, ultrashort, high-quality MeV-scale electron beams are opening opportunities into ultrafast electron microscopy and diffraction applications [4]. With more than 1400 industrial installations, electron-beam accelerators remain as the primary source of energetic electron beams for the above industrial processes [5].

Following its successful demonstration on several pilot projects [6], electron irradiation has garnered recent attention for high-volume applications such as municipal and industrial wastewater and sludge treatment. *E*-beam-based water treatment was successfully demonstrated as early as 1988 at the Miami-Dade Virginia Key wastewater treatment plant, where the process utilizing a 1.5 MeV *e*-beam at 50 mA (75 kW average power) successfully disinfected anaerobically digested sludge [7]. The plant achieved >99% removal efficiency for some organic compounds and ∼77% removal efficiencies for most compounds. In 1997, a pilot-scale *e*-beam treatment facility was commissioned at Daegu Dyeing Industrial Complex in South Korea. Initially specified for 1 MeV and 40 kW, the power was upgraded in 2005 to 400 kW. At 400 kW, the plant removed dye from 10 000 m^3 of wastewater per day [8]. In 2015, increased environmental regulation in Jiangsu Province, China led a wastewater treatment plant to investigate more advanced effluent remediation techniques. Proof-of-principle studies were performed with a Rhodotron TT200 electron accelerator at 10 MeV and 10 mA (100 kW of average power) [9]. Following success of this pilot, China opened the world's largest wastewater treatment facility at Guanhua knitting factory in Southern China. Though details on the *e*-beam

*rdhuley@fnal.gov

energy, current, and power have not yet been publicized as of the date of this paper, the facility is purportedly able to treat 30 million liters of industrial wastewater per day and save 4.5 billion liters of fresh water annually [10].

A recent study conducted at Fermilab [11] determined the requirements for 10 MeV *e*-beam power to treat 2 million gallons (∼8 million liters) of wastewater per day at the Metropolitan Water Reclamation District (MWRD) of Greater Chicago, one of the largest municipal wastewater treatment facilities in the United States. Nearly 1 MW of *e*-beam was deemed sufficient for treating dewatered biosolid sludge or the pre-anaerobic digester thickened waste activated sludge (WAS) stream in the MWRD Stickney plant at 2 million gallons per day (MGD). For the higher flow rate of 8–13 MGD of wastewater encountered upstream of WAS thickener, where there is a great opportunity to treat and recover water, *e*-beam power more than 5 MW is required. Both these applications can be well served by accelerator units delivering megawatt scale of 10 MeV *e*-beam.

Linear accelerators (linacs) using the room-temperature copper rf cavities are attractive for the MeV-scale energy range required for wastewater and sludge treatment. However, at higher frequencies (>250 MHz), these normal conducting rf cavities are constrained to operate at very low rf duty cycles due to high rf heating at the cavity walls potentially limiting their average *e*-beam power to a few tens of kilowatts. Superconducting rf cavities made of pure niobium or Nb_3Sn, with cryogenic operation near the temperature of 4 K, exhibit extremely small rf wall dissipation (about 6 orders of magnitude smaller than copper cavities of comparable shape and size), allowing their operation at 100% rf duty cycle (continuous wave or cw operation). SRF cavities can, thus, produce very high average power *e*-beams suitable for high-volume irradiation applications. For compact industrial applications demanding high average power (∼1 MW) at 10 MeV, SRF technology is an alternative approach to high-power linacs and could be more energy and cost efficient compared to copper cavities even after accounting for the energy and cost premium required for their cryogenic operation [12].

A prior publication by Ciovati *et al.* [13] reports a design of a 1 MeV, 1 MW SRF-based *e*-beam accelerator for the treatment of flue gases and wastewater. While the energy level of 1 MeV selected by Ciovati *et al.* is more suited for flue gas—a low-density material—a 10 MeV *e*-beam is more practical for treating higher-density materials such as wastewater and sludge. This is because the penetration depth of 10 MeV electrons in water is tenfold of 1 MeV electrons, which enables treating larger volume flows of water per unit time. Motivated by this striking advantage, we have designed a 10 MeV, 1 MW *e*-beam accelerator for high-volume (>MGD) wastewater treatment. The design and economic assessment (capital and operating expense) of this accelerator is the prime subject of the present paper.

The accelerator has a preaccelerator powered by a room-temperature electron source and an injector cavity. The main accelerator uses a scalable cryogenic module (cryomodule) in which a SRF cavity is conduction cooled using closed-cycle 4 K cryocoolers. Unlike conventional SRF cryosystems (see, for example, [14]), this technique makes use of neither large-scale helium cryogenic infrastructure nor complex liquid helium containing cryomodules. The technique offers the advantages of operational safety (less stringent loss of beam line vacuum [15,16]), simpler construction (simpler pressure vessel and pressure relief system), and reliability that are attractive for industrial settings.

This paper is structured to start with the design of the preinjector followed by the SRF cryomodule, including detailed beam dynamics simulations for attaining the 10 MeV, 1 MW final beam. We keep focus on the component-level engineering design of the SRF cryomodule, its assembly procedure, and then capital cost estimation. Finally, the accelerator wall plug efficiency and operating expense are estimated to evaluate the expected cost of wastewater treatment using beams produced by this accelerator.

II. ACCELERATOR DESIGN

A. Accelerator layout and components

Figure 1 depicts the major accelerator components and their layout. The layout is divided into three sections: preaccelerator, accelerator (also referred to as cryomodule), and beam delivery system. The preaccelerator is comprised of thermionic electron source (gun), an rf injector cavity, and a focusing solenoid magnet. The electron beam exiting the preaccelerator is fed into the accelerator, which energizes the beam to the 10 MeV target energy. The accelerator uses a Nb_3Sn (SRF) cavity operating near 4 K, conduction cooled by a bank of cryocoolers. The cavity cold mass is enclosed in a 50 K thermal intercept shield, surrounded by a room-temperature magnetic shield. The cavity cold mass and the two shields are housed in a vacuum vessel at room temperature. Two fundamental power couplers pierce the vacuum vessel through two ports at 180° to each other, to feed rf power into the SRF cavity. The beam exits the accelerator with 10 MeV energy and then enters the beam delivery system, where it is conditioned using a raster magnet and beam horn for irradiating a stream of wastewater. The electron-beam accelerator is ∼4 m long (end to end), ∼2 m wide, and ∼2 m tall.

B. Preaccelerator

The preaccelerator is composed of an electron gun, an injector cavity, and a focusing solenoid magnet arranged in the stated order. These components are designed to operate at room temperature and are situated outside of the cryomodule.

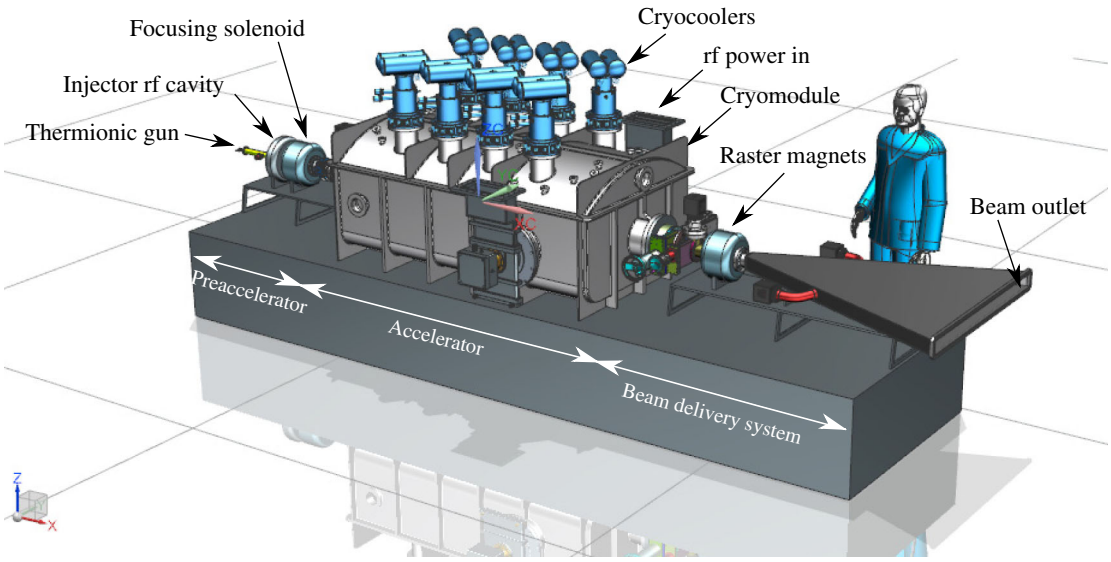

FIG. 1. *e*-beam accelerator components and layout. The overall size is ∼4 m long (end to end), ∼2 m wide, and ∼2 m tall.

1. Electron source (gun)

The preaccelerator herein uses a triode rf gun with a gridded thermionic cathode. In this gun, the cathode emits low-energy electrons via thermal emission, which are then shaped into electron bunches using the rf voltage applied to the grid-cathode gap, superimposed on a constant dc voltage. The emitted electrons are then captured and accelerated by the electric field of the rf gun. The operating rf amplitude and phase interval for the gun are determined for producing 100 mA average current with 154 pC electron-beam bunch charge. The 3D particle tracker software MICHELLE [17] is used for optimizing beam emittance, energy spread, and rms bunch length at the gun exit. The parameter summary of cathode and beam after the grid are presented in Table I. Figure 2 shows a cross section of the rf gun and its main components. Internal structural of the rf gun has three detachable parts: gun rf resonator with power coupler, thermionic cathode, and grid assembly. In the operating position, the grid's outside surface is directly facing the accelerating gap entrance of the injector cavity (described in the following section). The cathode unit is mounted to the rf gun resonator by a flanged connection and can be separated from the gun for maintenance. The standard series barium tungsten dispenser cathode with a diameter of 12.7 mm and operating temperature of 950–1200 °C is considered for the present study. Bellows are used as part of the outer conductor of the rf gun for mechanical adjustment of the cathode-grid distance.

TABLE I. Parameters of the 650 MHz rf gun with thermionic cathode.

Gun parameter	Value
Cathode diameter	12.7 mm
Current density	2.35 A/cm^2
Cathode temperature	950–1200 °C
dc bias voltage	2.6 kV
Output energy	3.5 keV
Bunch rms size	<15°
Energy rms size	<25%

2. Injector cavity rf design

The injector cavity, located immediately downstream of the rf gun, captures the thermionically emitted electrons and accelerates them to ∼300 keV energy. The rf design of the injector cavity is done using CST Microwave Studio software. The goal of cavity RF design is to maximize the shunt impedance to get the required accelerating voltage with minimum heat dissipation. The main dimensions for optimization are longitudinal length L_{cavity}, accelerating gap length L_{gap}, and the radii R_1 and R_2 as depicted in Fig. 3. The cavity diameter is chosen to attain TM010 mode

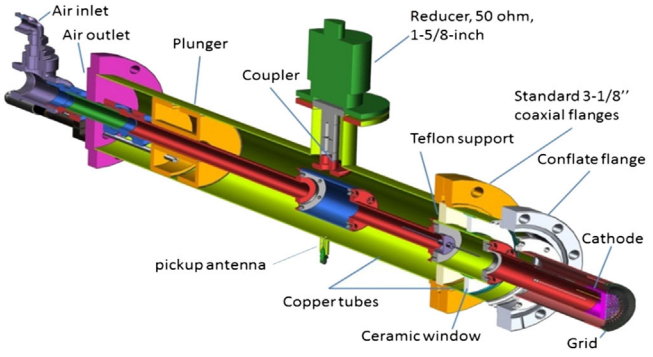

FIG. 2. The rf gun design parameters (left) and components (right).

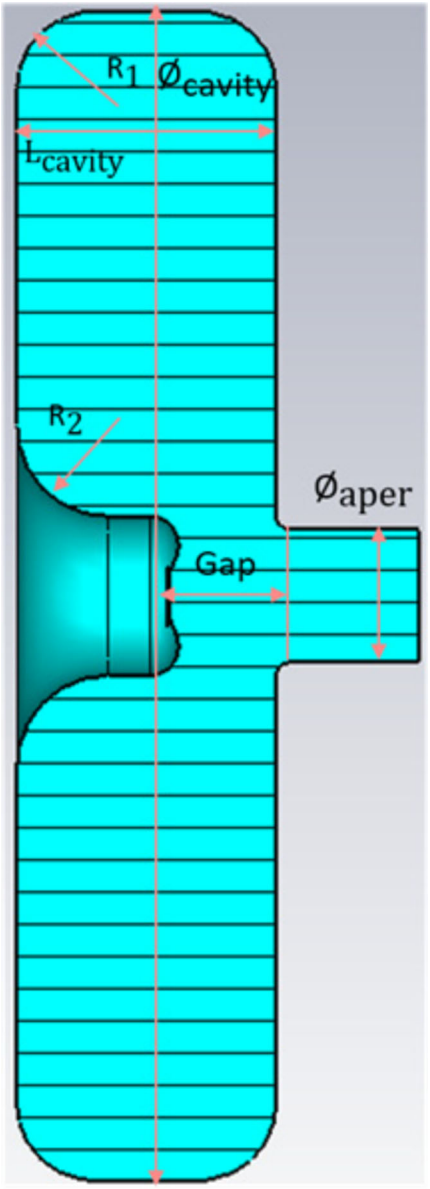

FIG. 3. Injector cavity design and operating parameters.

resonance at 650 MHz. The optimized geometrical dimensions and the resulting rf parameters are also summarized in Table II. Taking copper as the injector cavity material, the voltage gain of ~300 kV would dissipate 11.6 kW of heat, which can be extracted using forced flow of cooling water around the cavity.

3. Beam dynamics simulations of the rf gun and injector cavity

The simulation of the electron emission for the cathode-grid region with the rf gun resonator was carried out with MICHELLE. The control cathode voltage has the following time dependence:

TABLE II. Parameters of the 650 MHz rf gun with a thermionic cathode.

Dimension	[mm]	rf parameter	Value
ϕ_{cavity}	308	V_{out}	300 kV
ϕ_{aperture}	35	r/Q	178 Ω
R_1	20	Q_0	19 000
R_2	24	R_{shunt}	3.4 MΩ
L_{gap}	29.6	rf loss	11.6 kW
L_{cavity}	68.2	$E_{s,\text{max}}$	14.5 MV/m

$$U(t) = U_d + U_a \cos(\omega t + \phi), \tag{1}$$

where U_d is constant bias voltage, U_a is amplitude of the bias rf voltage, ω is rf frequency, and ϕ is phase shift between the bias rf field in the injector and rf field in the gun cavity. For the optimization, we varied U_d, U_a, and ϕ as well as injector voltage to obtain the required average current $I_{\text{avg}} = 0.1$ A and 0.3 MeV beam output energy and to minimize bunch length rms and beam energy spread rms. Figure 4 shows MICHELLE plots of emitted particles at the time of the beginning of emission from the cathode surface and the $\beta\gamma$ distribution of the beam at the moment of its propagation through the middle of the injector gap. The simulations use a quarter model of the gun owing to symmetry. The calculated beam characteristics and particle distributions at the exit of the injector cavity are summarized in Fig. 5. A beam spot size of ~12 mm diameter is obtained at the exit of the injector cavity.

4. Focusing solenoid

The focusing solenoid operating at room temperature is used to match the beam transverse optics to the SRF cavity. The solenoid should (a) provide required focusing properties, (b) be compact, and (c) being placed close to the SRF cavity, should create only a small remnant magnetic field (a few mG) on the cavity surface to avoid reduction in its quality factor Q_0. The solenoid is placed at the distance of ~300 mm upstream of the SRF cavity to avoid bunch lengthening, requiring it to provide 0.3 m of focusing distance. This translates to the solenoid having the length of ~100 mm, providing a field of 200–250 G. Hence,

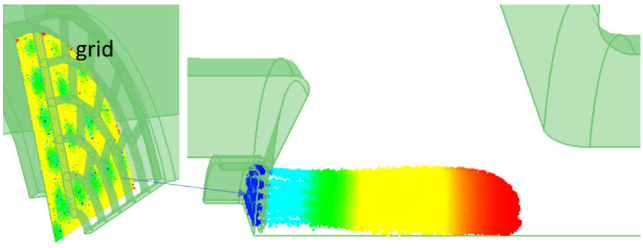

FIG. 4. Beam distribution at the time of emission from the cathode and $\beta\gamma$ beam distribution in the middle of the injector gap.

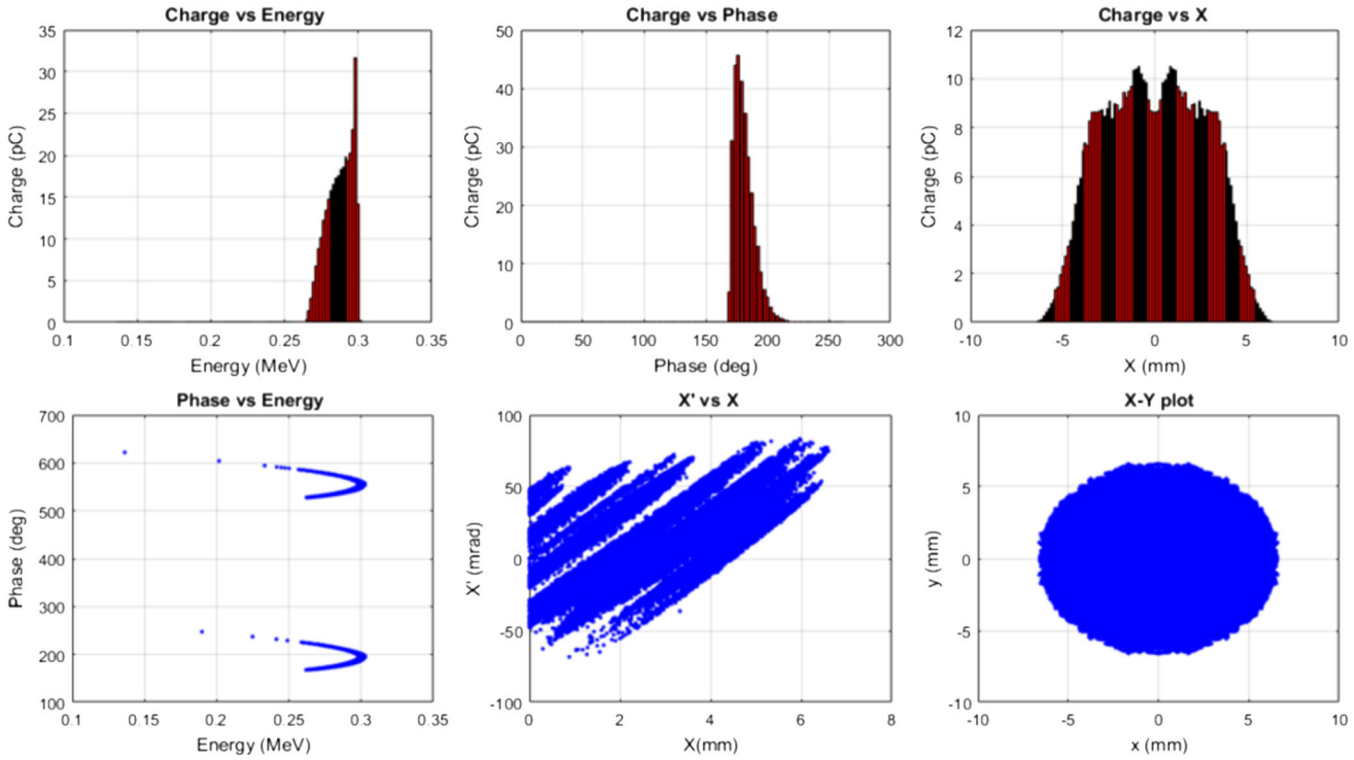

FIG. 5. Beam characteristics at the exit of the injector cavity. Top three plots: charge distribution vs energy and phase and current vs radius. Bottom three plots: phase vs energy, $x' - x$ phase-space distribution, and $x - y$ plot at the injector exit.

focusing strength is of about 6×10^{-5} T^2 m. Table III presents the solenoid design parameters that produce the required field profile and focusing strength. The required solenoidal field profile generated by an electromagnetic solenoid with the dimensions in Table III is shown in Fig. 6.

C. Main accelerator cavity rf design and beam transport simulations

1. Cavity rf design

Figure 7 shows geometrical dimensions of the five-cell, 650 MHz cavity designed to produce the 10 MeV electron beam. The cavity inlet port has 35 mm diameter, equal to that of the injector cavity outlet. This is much larger than the beam spot size of ~12 mm at that location. To match the phase of low-beta electrons entering the cavity, the first cell of the cavity has shorter length compared to the other four cells. Cells 2–4 have the same length and diameter, while the fifth cell is longer and larger in diameter. The outlet iris of the fifth cell and the downstream beam pipe are also larger in diameter compared to the other four irises. This larger size is chosen to achieve adequate coupling of the fundamental power coupler with the five-cell cavity as well as outpropagation of any higher-order modes. The outlet beam pipe has two coupler ports, placed 180° from each outer, for feeding rf power to the cavity. The beam pipe diameter downstream of the coupler port location is reduced to match the diameter of the beam delivery system.

TABLE III. Parameters of the focusing solenoid at the accelerator inlet.

Solenoid parameter	Value
Coil ID/OD	50/120 mm
Coil length	90 mm
Peak field on axis	0.025 T
Current density	0.4 A/mm^2
Focusing strength	6×10^{-5} T^2 m

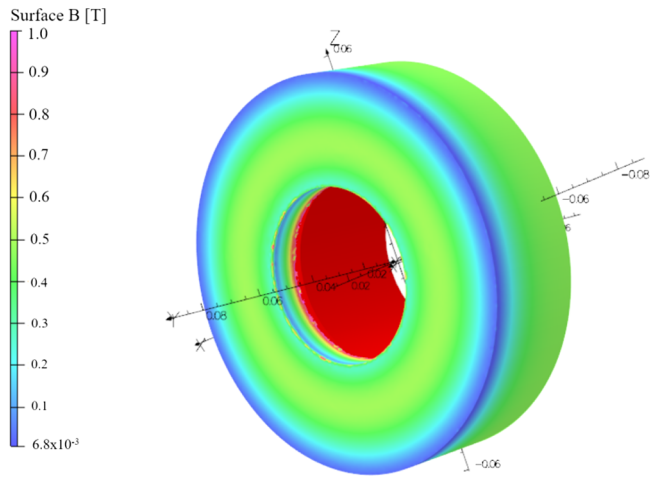

FIG. 6. Surface magnetic field produced by the solenoid (dimensions in meters).

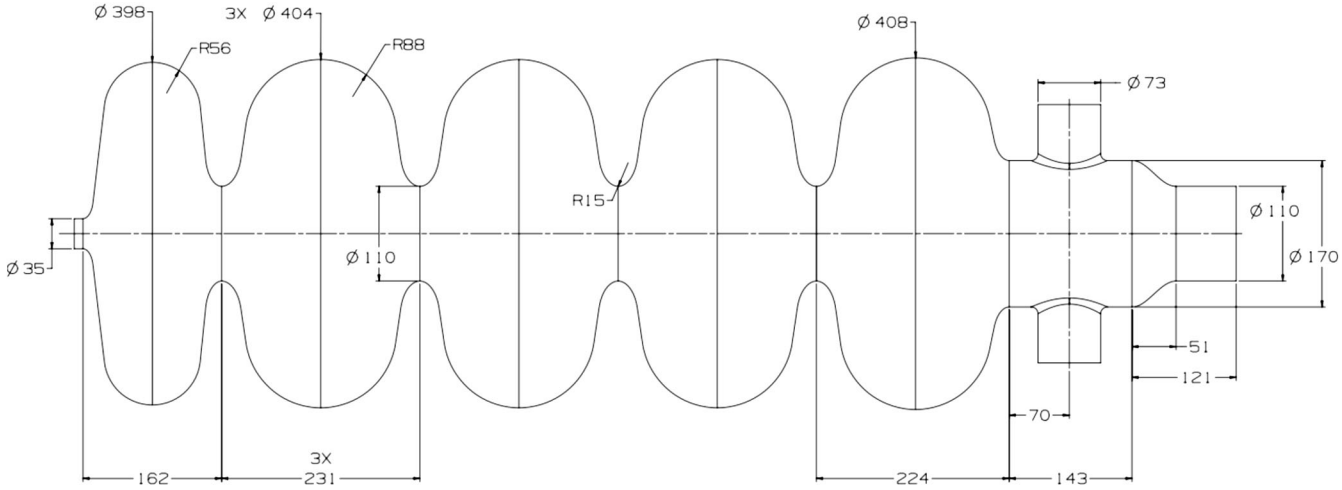

FIG. 7. Geometrical dimensions of the five-cell cavity rf volume. All dimensions are in millimeters.

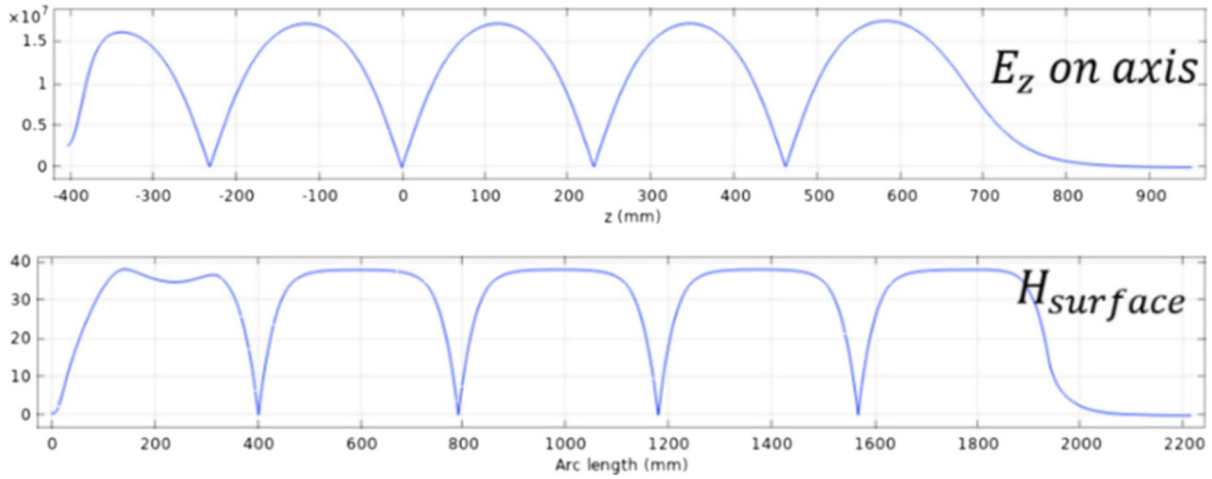

FIG. 8. Axial electric and surface magnetic field for the five-cell cavity at 10 MV voltage gain.

The geometrical dimensions shown in Fig. 7 are obtained via coupled rf and beam transport optimization of the cavity to maximize the quantity $G * R/Q$ for the required 10 MeV voltage gain. This maximization ensures minimum heat dissipation for a given surface rf resistance R_s. The optimization also considers obtaining reasonable peak field ratios and good flatness of the surface magnetic field. The calculated axial electric field and surface magnetic field profiles at 10 MV voltage gain are depicted in Fig. 8. The optimization produced a uniform axial field profile and flat surface magnetic field profile in each of the five cells. Table IV lists the optimized rf parameters of the cavity. The total cavity length is 1.35 m, of which 1.08 m is the accelerating length.

2. Coupler side cavity end-group design

As previously stated, the diameter of the fifth cell and outlet beam pipe is enlarged compared to the regular cavity iris from 110 to 170 mm to allow (a) for outpropagation of higher-order modes (HOMs) and (b) achieve high cavity coupling with the fundamental power couplers. It is also necessary to ensure a sufficiently small operating value of the $Q_{\text{ext}} \sim 1.5 \times 10^5$ and simultaneously avoid proximity of the antenna tip to the beam axis. The shape of antenna tip that balances these two opposing requirements is shown in

TABLE IV. Parameters of the optimized 650 MHz five-cell SRF cavity.

Cavity parameter	Value
Normalized shunt impedance R/Q	635 Ω
Geometry factor G	262 Ω
Dissipated power P_{diss} at 10 MeV	$0.6R_s$ [nΩ] W
Peak surface electric field $E_{s,\text{peak}}$	17.5 MV/m
Peak surface magnetic field $B_{s,\text{peak}}$	36.5 mT

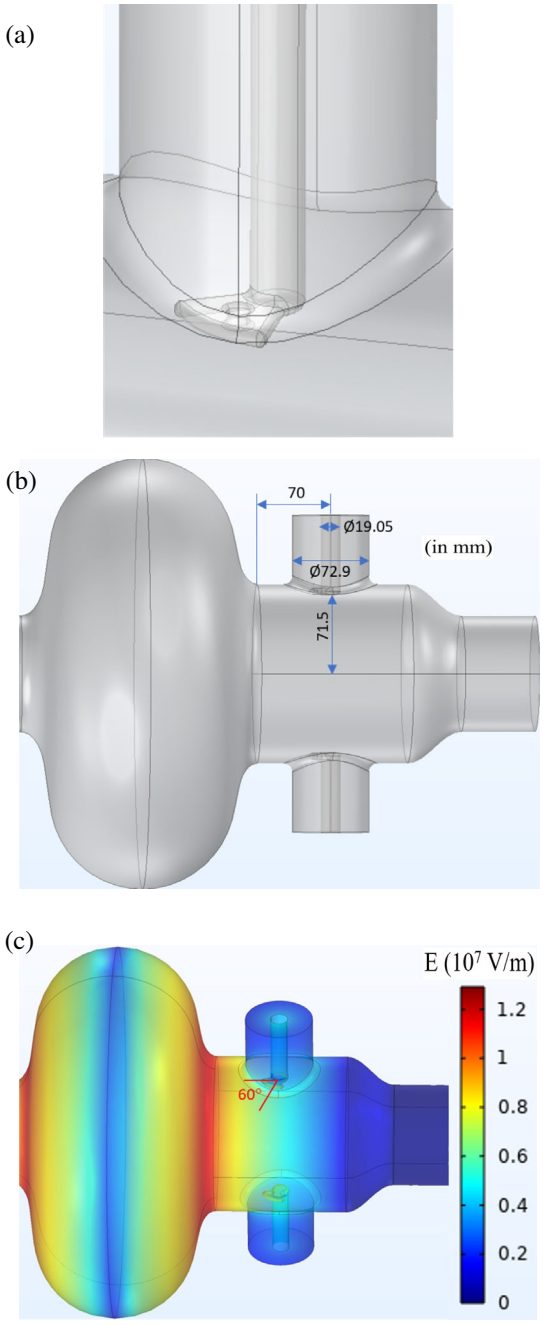

FIG. 9. Five-cell cavity coupler-side end-group (a) enlarged view of coupler antenna tip, (b) dimensions of power coupler port and antenna position, and (c) electric field distribution in the cavity end group.

the plot in Fig. 9. A 180° rotation of the antenna tip brings the Q_{ext} in the range of 1–2.5 × 10^5 that includes the target $Q_{\text{ext}} \sim 1.5 \times 10^5$. The antenna tip is oriented 60° with the cavity beam axis as depicted in Fig. 9(a) and located 71.5 mm from the beam axis to attain the required Q_{ext}. Figure 9 also shows the main dimensions of the fundamental power coupler port and antenna position and electric field distribution in the cavity end group.

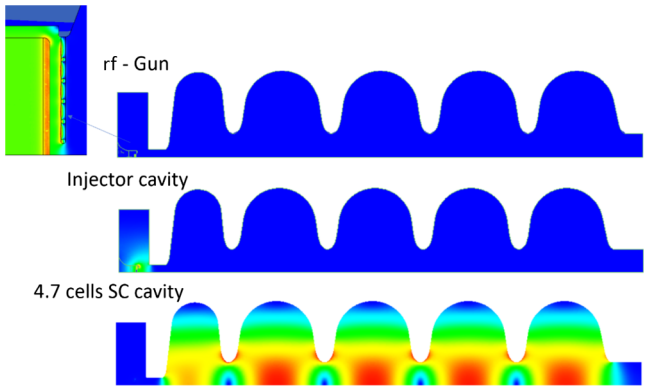

FIG. 10. The three sets of EM fields used for MICHELLE simulation of beam transport through the accelerator.

3. Simulation of beam transport through the cavity

The optimized bunch distribution at the output of the injector cavity is used at the entrance of the five-cell SRF cavity to simulate the bunch acceleration through the five-cell cavity. This assumes negligible bunch distortion between the output of the injector cavity and inlet of the five-cell cavity, facilitated by the focusing solenoid. Note that under this assumption we have excluded the focusing solenoid from beam transport simulations. Three sets of fields as shown in Fig. 10 are used in MICHELLE beam transport simulations. The amplitude and phase shift in the five-cell cavity are matched to obtain the 10 MeV beam at the outlet of the accelerator.

Using up to 100 000 particles and neglecting particle loss to cavity walls, the MICHELLE simulations confirmed that the five-cell cavity depicted in Fig. 7 produces uniform acceleration in each cell, starting from 0.3 MeV at the injector outlet and ending in 10 MeV at the five-cell cavity outlet. The progressive bunch energy gain through the cavity cells and beam parameters used in the simulation are summarized in Fig. 11. Finally, the beam characteristics and particle distributions at the exit of the five-cell cavity are summarized in the plots in Fig. 12.

4. Analysis of HOMs

An understanding and mitigation of cavity HOMs is essential to ensure proper beam transport through the

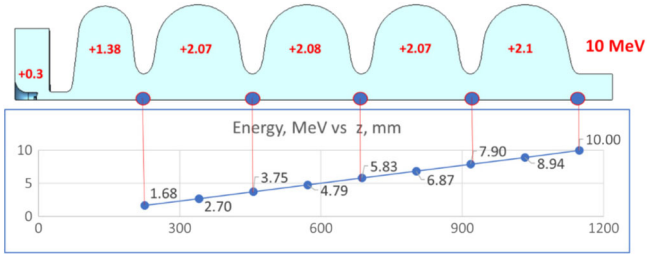

FIG. 11. Beam transport through the five-cell SRF cavity: cell-by-cell bunch energy gain (left) and output beam parameters (right).

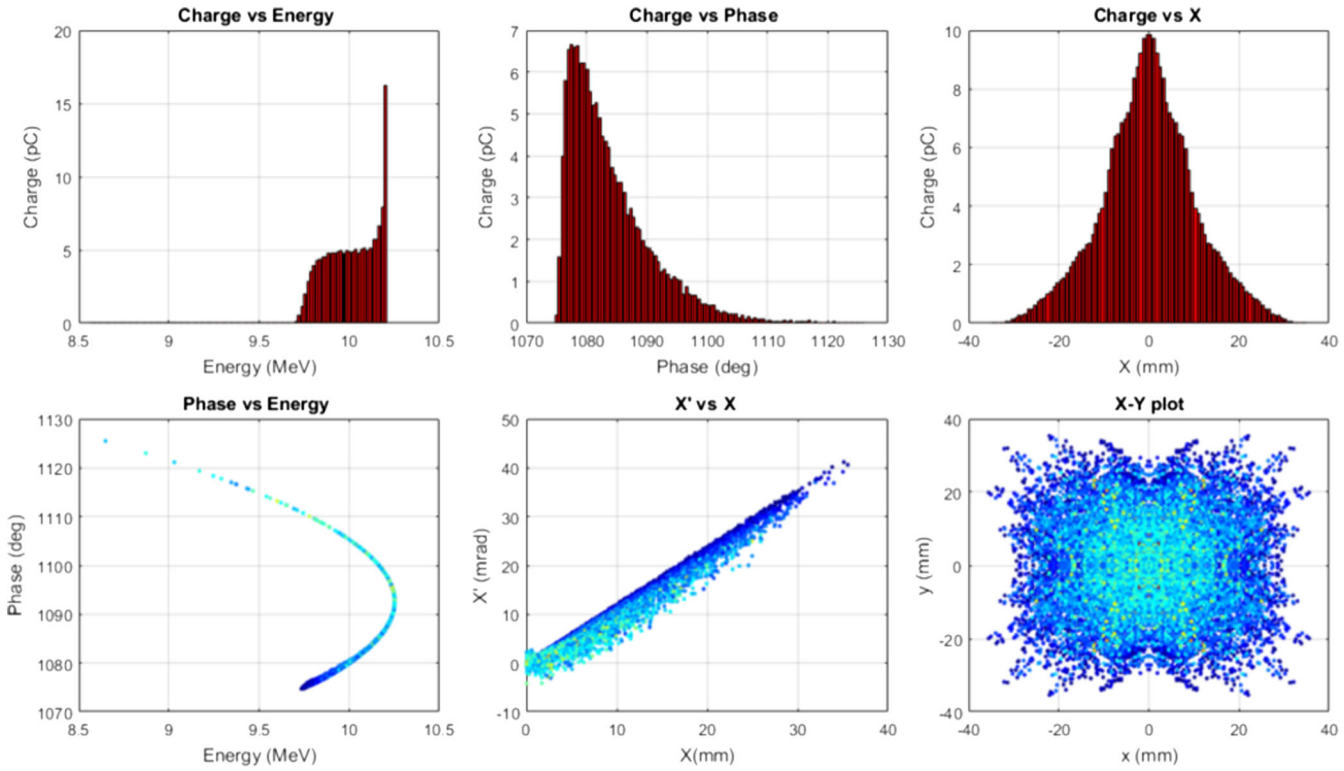

FIG. 12. Beam characteristics and particle distributions at the exit of the five-cell cavity. Top plots: charge distribution vs energy and phase and current vs radius; bottom plots: phase vs energy, $x' - x$ phase-space distribution, and $x - y$ beam spot size.

cavity. In this section, we present the calculated cavity HOM spectrum including monopole and dipole modes and discuss their impact on beam transport through the cavity.

Cavity HOM spectrum.—The monopole and dipole HOM spectrum of the five-cell cavity shown in Fig. 13 are calculated by eigenmode simulations in CST Microwave Studio. Most "dangerous" monopole modes are close to the bunch frequency of 650 MHz. However, these HOMs have only 1% normalized impedance, $(r/Q)_{\text{monopole}}$ of that of the fundamental frequency. All other monopole HOMs are far away from harmonic multiples of the fundamental frequency and also have relatively small $(r/Q)_{\text{monopole}}$. We therefore conclude that the monopole HOM excitation will not have a drastic effect on bunch acceleration. Similarly, all the dipole HOMs are far away from the fundamental of 650 MHz as well as the second harmonic of 1300 MHz. Thus, dipole HOM excitation is also expected to be insignificant.

HOM analysis model.—The present HOM model considers a continuous train of pointlike bunches passing through the five-cell cavity and accelerated by the cavity voltage. Bunch frequency is $f_b = 650$ MHz, and each bunch has a charge of $q_b = 154$ pC. Energy gain of bunches at the exit of the cavity is 10 MeV. Each passing bunch induces decelerating voltage in monopole mode k, given by

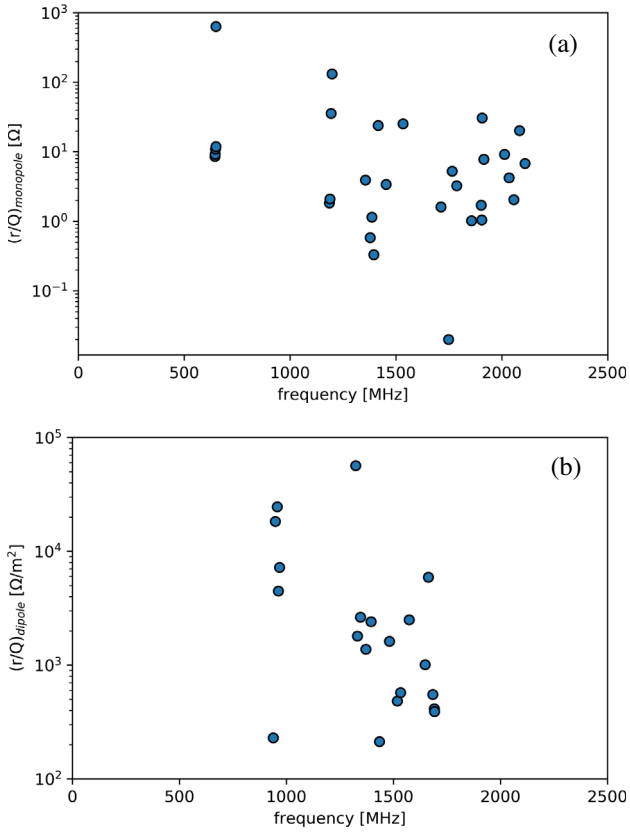

FIG. 13. Impedances of (a) monopole HOMs and (b) dipole HOMs as a function of the mode frequency.

$$U_k^{||} = -(1/2)(r/Q)_k \omega_k q_b, \tag{2}$$

where $\omega_k = 2\pi f_k$ and $(r/Q)_k$ are circular frequency and impedance of mode k, respectively. According to the Wilson theorem of beam loading, the bunch sees half of its induced voltage. As the bunch passes through the cavity, the induced voltage evolves with time according to

$$U_k^{||}(t) = U_k^{||} \exp[(j - 1/2Q_k)\omega_k t]. \tag{3}$$

The total longitudinal voltage seen by bunch N from the beginning of the bunch train is then given by

$$V_N^{\mathrm{HOM},||} = \mathrm{Re} \sum_{k=1}^{P} U_k^{||} \left(\frac{1}{2} + \sum_{n=1}^{N-1} \exp\left[\left(j - \frac{1}{2Q_k} \right) \frac{\omega_k n}{f_b} \right] \right), \tag{4}$$

where P is the total number of monopole modes, excluding the accelerating mode. If bunches have transverse displacement x_b from the cavity axis, they also excite dipole modes. The induced transverse "kick" voltage is given by

$$U_k^{\perp}(t) = \frac{1}{2} j c q_b (r/Q)_{\perp} x_b, \tag{5}$$

where c is the speed of light. Total transverse kick voltage seen by bunch N from Q dipole modes is calculated as the following:

$$V_N^{\mathrm{HOM},\perp} = \mathrm{Re} \sum_{k=1}^{Q} \sum_{n=1}^{N-1} U_k^{||} \exp\left[\left(j - \frac{1}{2Q_k} \right) \frac{\omega_k n}{f_b} \right]. \tag{6}$$

Finally, the bunch transverse deflection angle as the ratio of kick voltage to total longitudinal momentum is given by

$$X'_N = \frac{V_N^{\mathrm{HOM},\perp}}{(pc)_{||}}. \tag{7}$$

Figure 14(a) shows longitudinal voltage excited in monopole modes. Black markers show bunch-by-bunch voltage, green markers show cumulative mean voltage value, and red markers show cumulative rms voltage value. The main contribution to longitudinal voltage is due to mode 4: 649.4 MHz. Quasiperiodic oscillations are at 0.6 MHz, the frequency difference between bunch and mode frequencies. Maximum longitudinal voltage during transition is less than 1 kV, which is very small compared to cavity voltage 10 MV. Results for dipole modes excited by bunches with 1 mm transverse displacement are shown in Fig. 14(b). Quasiperiodic oscillation is at 23.9 MHz (frequency difference between dipole mode 6 and first beam frequency harmonic). Maximum kick voltage from dipole modes during transition is −13 V. This is extremely small compared to longitudinal momentum. The corresponding transverse deviation angle is ∼0.001 mrad.

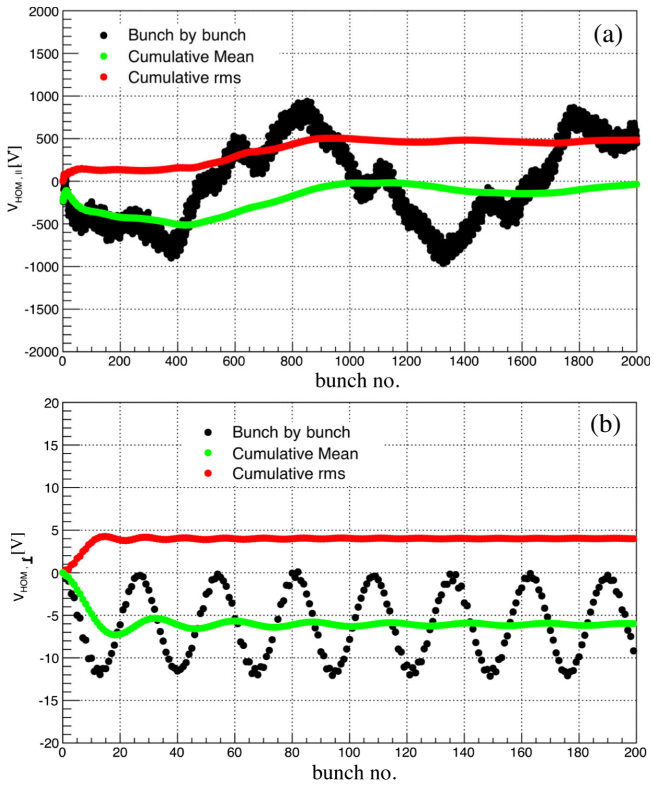

FIG. 14. (a) Monopole HOM voltage and (b) dipole HOM voltage for the five-cell 650 MHz cavity.

We note that both longitudinal and transverse voltage are proportional to the beam current. If we assume that effects of HOMs should not exceed 0.1% on longitudinal and 0.1 mm on transverse beam dynamics, we still have at least a factor of 10 margin on beam current. Therefore, we conclude that HOMs are not expected to be an issue for the five-cell cavity.

D. Design of fundamental power coupler

The rf power is fed to the five-cell SRF cavity using two couplers, each sustaining 500 kW cw power with ∼10% reflection. The coupler design is presented in this section, focusing on its rf performance, structural strength, and cryogenic loading to 4 K. The present design is motivated by the 650 MHz couplers developed and tested for the Proton Improvement Plan II (PIP-II) accelerator [18]. This design uses a ceramic window to separate the air side of the coupler that receives power from an rf source, from the vacuum side that delivers power to the cavity.

1. Ceramic window

The ceramic window configuration as depicted in Fig. 15 has 100 mm outer diameter, 25.4 mm inner diameter, and 7 mm thickness. The disk is made of alumina with a loss

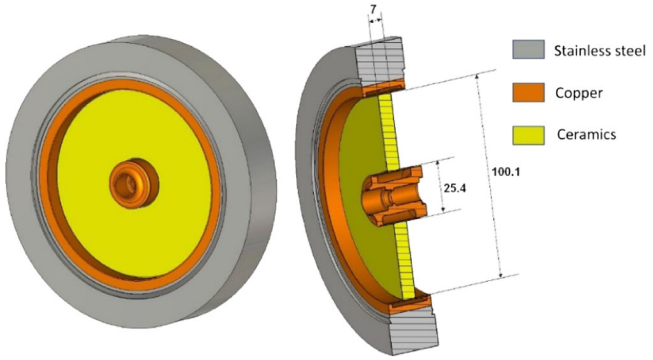

FIG. 15. Configuration and dimensions of the coupler ceramic window.

tangent of 10^{-4} or less and is brazed with the outer and inner copper bushings. The outer copper bushing is brazed with a stainless-steel ring that connects to the outer conductor of the coupler.

2. Mechanical design of the power coupler

The principal components of the coupler as assembled are depicted in Fig. 16. To reduce static and dynamic cryogenic loading to 4 K, the coupler uses a copper electromagnetic shield (EMS) heat sunk only at ∼50 K and no physical contact with the cavity. The EMS screens the stainless-steel outer conductor, aluminum gasket, and stainless flange from the electromagnetic field, thereby reducing Ohmic losses in the outer conductor, gasket, and flange. All rf losses are mostly concentrated in EMS and are intercepted by the 50 K thermal intercept. The EMS also includes an iris to reduce thermal radiation from room-temperature ceramic and protects the ceramic window from charged particles that can come from the cavity. The inner conductor of the coupler is a hollow copper channel cooled with a forced flow of water.

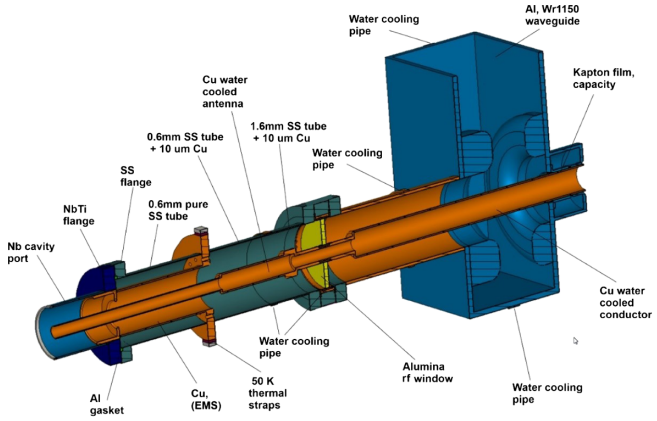

FIG. 16. Cut view of configuration of 650 MHz, 500 kW, cw coupler.

3. Thermal analysis of the power coupler

Thermal analysis is conducted to estimate cryoloading (Ohmic losses) in the coupler under steady operation with 500 kW forward propagation. The analysis uses the configuration and materials shown in Fig. 17. The outer conductor is made of stainless steel with 0.6 mm wall thickness. The air side of the outer conductor (to the right of the 50 K intercept) is coated with 10 μm copper, while the vacuum side (to the left of the 50 K intercept) is pure stainless steel, shielded by the EMS. A part of the EMS penetrates the cavity port made of superconducting niobium at 4 K. There is a 0.8 mm gap between the EMS and port wall to prevent thermal contact. All the EMS Ohmic losses are intercepted at 50 K. The antenna, inner conductor, ceramic disk, and the air side of the outer conductor are cooled with a forced flow of water at 300 K. The outer copper sleeve of the ceramic window is cooled by water as well. The metal electrical conductivities and dielectric loss tangent of nonmetals used in the thermal analysis are stated in Fig. 17(a). Figure 17(b) shows the coupler temperature map at steady 500 kW of forward propagation with 10% reflection, and the componentwise losses are listed in Table V. With water cooling, the antenna tip is expected to operate at ∼312 K. The conduction heat leak to the cavity port at 4 K is determined to be 0.6 W. In addition to this conductive heat leak, the cavity port will also experience incident radiation heat transfer from the warm EMS and the antenna tip. A finite element calculation of radiation heat transfer to the cavity coupler port using the temperature distribution in Fig. 16(b) showed this

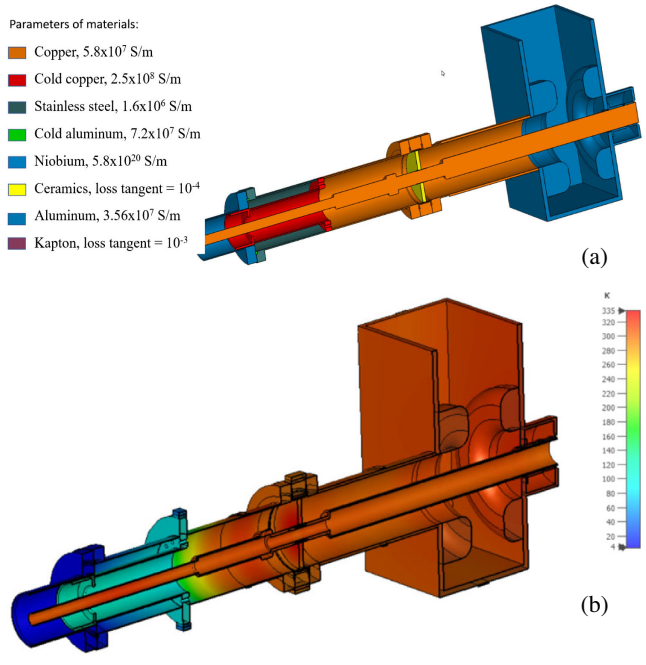

FIG. 17. Thermal analysis of the fundamental power coupler at 500 kW forward propagation (a) geometry and material properties and (b) steady-state temperature map.

TABLE V. Losses in the coupler components for 500 kW forward propagation and 10% reflection.

Component	Loss [W]	Loss extracted by
Outer conductor and flange to cavity port	0.6	Cavity port, ~4 K
Al gasket at the cavity port	1.5×10^{-3}	
EMS	31.5	Thermal intercept, ~50 K
Outer conductor (vacuum side), upstream of 50 K intercept	29.5	
Antenna	570	Cooling water, ~300 K
Ceramic disk	43	
Kapton	5.5	
Outer conductor (air side)	44	
Al waveguide	255	

additional load to be ~0.55 W. Therefore, the total 4 K heat load to the cavity port is expected to be ~1.2 W at full coupler forward power.

4. Multipacting analysis of the power coupler

The vacuum side of the power coupler is analyzed for multipacting issues, which are then mitigated by applying a dc bias. The vacuum side is divided for four sections, and each section is simulated for multipacting with and without dc high-voltage bias. The simulations are done for 866 kW, pure TW rf power, which is "field" equivalent of 500 kW, 10% reflection. The four sections and a representative graph of rise of particles number vs time are presented in Fig. 18. Although multipacting is seen to exist in all the sections, it can be suppressed by applying a 5–6 kV dc bias.

5. Summary of coupler design

The main design parameters of the fundamental power coupler are summarized in Table VI. With the use of the EMS, we find that the 4 K loading can be restricted to ~1.5 W at 500 kW of forward rf power. With two such power couplers, the total 4 K heat load is expected to be ~3 W.

E. Accelerator cryomodule design

A cross section along the beam line of the cryomodule assembly is shown in Fig. 19. The cryomodule includes a vacuum vessel, a 650 MHz Nb_3Sn cavity, eight two-stage cryocoolers (four on each side of the beam line as seen in Fig. 19), and single-layer thermal and magnetic shields. The cavity is conduction cooled to the cryocoolers as will be described later in this section. The thermal shield insulates the SRF cavity from ambient thermal radiations and intercepts the heat transmitted through the rf couplers and the beam line ports. The thermal shield is connected to

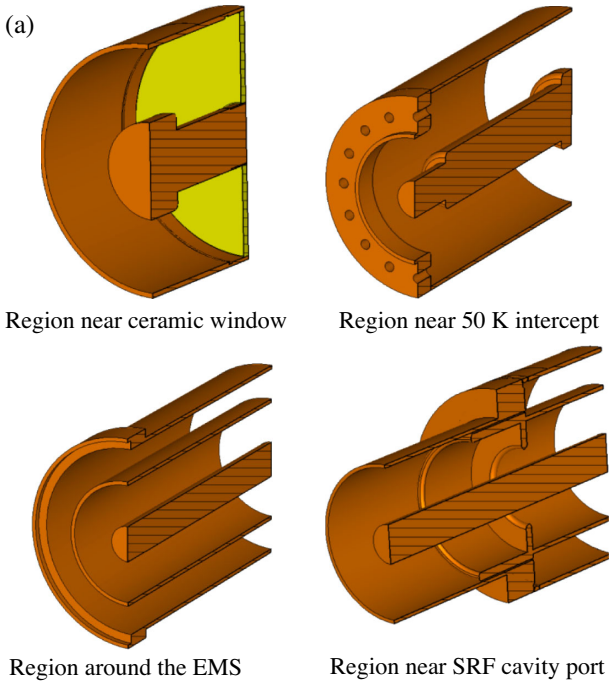

FIG. 18. (a) Vacuum side coupler sections analyzed for multipacting and (b) representative observation of multipacting and mitigation by applying dc bias. A similar plot is obtained for each section but not shown here to avoid clutter.

the 50 K cooling stage of the cryocoolers using a set of thermal straps [19] visible in Fig. 19. Two types of cryocoolers are selected: six Cryomech PT420 offering a cooling capacity of 2.0 W at 4.2 K and two additional Cryomech PT425 with a higher cooling capacity of 2.5 W at 4.2 K located above the rf couplers. Pulse tube (PT) coolers are chosen over Gifford McMahon (GM) coolers, because PTs do not have moving parts at the cold end. The absence of moving parts improves the mean time between maintenance and reduces vibrations that can cause cavity microphonics. PTs have lower energy efficiency than GMs, but, as is shown in Sec. III, this penalty is not expected to

TABLE VI. Summary of the 650 MHz power coupler design parameters at 500 kW forward power.

Coupler parameter	Value
Cryogenic loading to 4 K	1.5 W
Cryogenic loading to 50 K	62 W
Losses in ceramic window	32 W
Max temperature at ceramic window	335 K
Max temperature at antenna tip	312 K
Bias voltage for suppressing multipacting	5–6 kV dc

affect the overall efficiency of the accelerator. This is because the overall efficiency is dominated by the rf power source.

Strong magnetic fields can impair the intrinsic quality factor of the cavity, thereby reducing the attainable accelerating gradient for a given cryocooling capacity. A magnetic shield is provided to limit the total magnetic field on the surface of the SRF cavity to <10 mG. The magnetic shield is operated at room temperature to avoid additional cryogenic loading of the cryocoolers. The cold mass and the magnetic shield are all enclosed in a 1.95-m-long vacuum vessel. The total mass of the fully assembled cryomodule is estimated to be 1750 kg. The design and analysis of the various cryomodule components are presented in the following sections.

1. SRF cavity cooling design and thermal analysis

Estimation of SRF cavity cryoloading.—Table VII presents the calculated ~4 K heat load on the cavity and the details of the cryocoolers chosen to provide the required cooling load. The cavity is divided into two sections to simplify the heat load estimation: (i) the main body comprising the five elliptical cells and the inlet beam tube and (ii) the outlet side made of the two coupler ports and outlet beam pipe. The static heat leak contributions of thermal radiation from the thermal shield and via beam pipes, thermal conduction via cavity supports, beam pipes, and coupler ports are considered. The dynamic loading comprises beam loss, cavity rf heating, and coupler loading. Although not explicitly determined in this study, we take a beam loss of 1 W (as estimated in a previous study [11]), which is 1 ppm of the average beam power. The cavity rf heating is initially estimated using 20 nΩ surface resistance for the Nb_3Sn rf surface at 650 MHz and 10 MV voltage gain over the five-cell cavity length (see Table IV for the expression of dissipated rf power). The rf heat load will be revised in a subsequent section by accounting for the temperature dependence of Nb_3Sn surface resistance. While the total heat load from the couplers to the cavity was previously estimated to be ~3 W (~1.5 W per coupler; see Table VI), we take a conservative value of 3 W per coupler as seen in practice with a 500 kW coupler designed at Brookhaven National Laboratory (BNL) [20]. Note that the present study does not use the BNL coupler, just its reported value of heat leak to ~4.2 K. In summary, the total cavity heat load is estimated to be 19.5 W. The cavity body and inlet side experiences 14 W of heat load, which can be extracted using six Cryomech PT420 cryocoolers operating at 4.45 K. The cavity outlet side has 6.5 W of cryoloading, which is manageable using two Cryomech PT425 cryocoolers operating at 4.6 K.

SRF cavity cooling design and analysis.—The five-cell cavity shown in Fig. 20 is made of a 4-mm-thick niobium shell (SRF grade, RRR > 300) around the profile given in Fig. 7. The cavity inner surface is coated with a

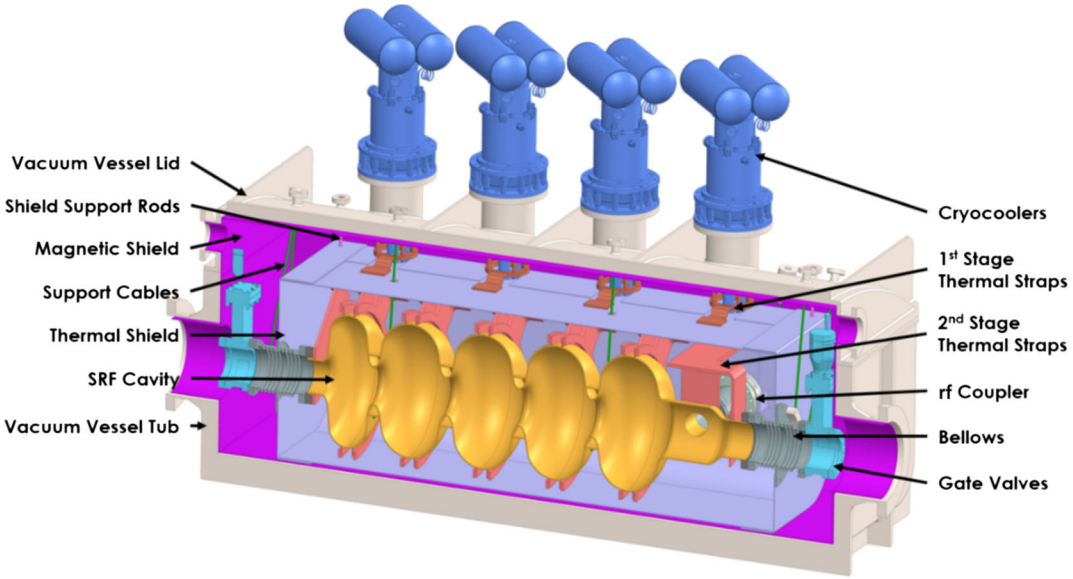

FIG. 19. Cross-section view of the SRF cryomodule assembly. The end-to-end length is 1.95 m.

TABLE VII. Calculated heat load on the 5-cell SRF cavity.

Cavity parameter	Heat load	Value [W]	Cryocooler selection
Cavity body	RF dissipation @ 10 MeV and $R_s = 20$ nΩ	12.5	
	Radiation from thermal shield	0.05	
	Beam loss (taken as 1 ppm of average beam power [11])	1	
	Conduction through supports	0.1	
Cavity inlet	Conduction through inlet beampipe	0.05	
	Radiation from inlet port [25]	0.24	
Cavity body + inlet		14	6x Cryomech PT420, cooling capacity 14.3 W @ 4.45 K
Cavity outlet	Couplers [20]	6	
	Conduction through outlet beampipe	0.05	
	Radiation through outlet beampipe [25]	0.04	
Cavity outlet		6.3	2x Cryomech PT425 cryocoolers, cooling capacity 6.5 W @ 4.6 K
Total		19.5	

~2-μm-thick layer of Nb_3Sn, which enables low dissipation operation at ~4 K temperature. Each cell has two 4-mm-thick conduction cooling rings made of SRF-grade niobium that are *e*-beam welded at about 12.5 mm on either side of the cell equator. The two coupler pipes as well as the inlet and outlet beam pipe carry thermal intercepts made of niobium. All the port flanges are made of niobium-titanium alloy and are *e*-beam welded to the beam and coupler ports.

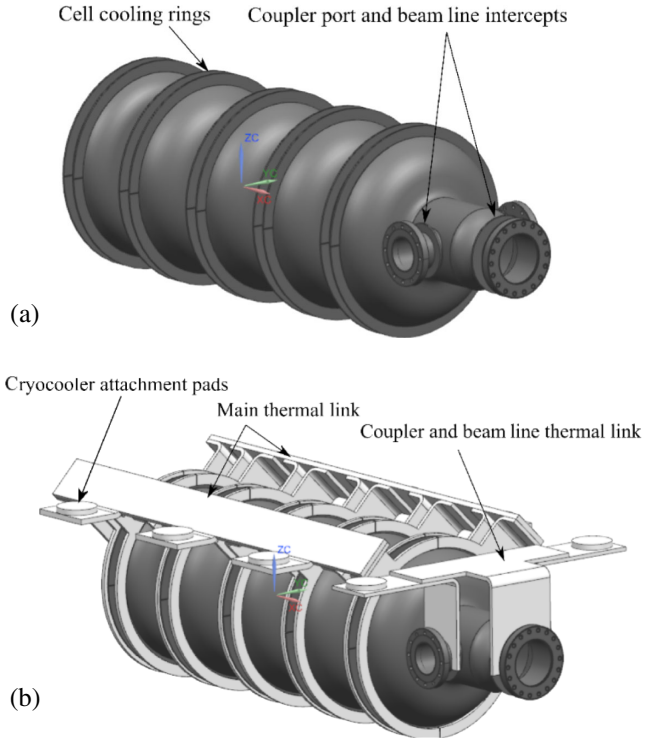

FIG. 20. (a) Rendering of the five-cell cavity with *e*-beam welded cooling rings and (b) thermal links attached to the five-cell cavity by bolting.

High-purity (5N or 99.999% pure) aluminum thermal links are used to conductively connect the five-cell niobium cavity with the cryocoolers. Two separate thermal links are used—one for cooling the inlet beam pipe and the five cells and the second for cooling the outlet beam pipe and coupler pipes. The link components are cut out of 4-mm- or 6.35-mm-thick sheets of commercial 5N aluminum and then bent into final shapes. The components are then connected to each other and to the cavity cell cooling rings, resulting in the configuration depicted in Fig. 20. All the connections within the link as well as to the cavity are made using off-the-shelf nuts, bolts, and disk springs that enable easy disconnection if required. Although not shown in Fig. 20 to avoid clutter, the niobium rings on the cavity cells carry several bolt holes to connect with the aluminum thermal link components.

The effectiveness of the aluminum thermal links is evaluated by systematic finite element simulations. The goals here are (i) to obtain reasonably small temperature drop between the cavity rf surface and the cryocoolers and (ii) to obtain reasonably uniform surface temperature of the cavity. The simulations use the following two heat transfer boundary conditions: (i) all heat flows at appropriate locations on the cavity as listed in Table VII and (ii) temperature-dependent cooling capacity of the cryocoolers (measured in house), imposed on the cryocooler attachment pads. The simulations use temperature-dependent Nb_3Sn surface resistance (taken as the sum of 20 nΩ residual and BCS resistance calculated using SRIMP [21]), temperature-dependent thermal conductivities of 5N aluminum [22] and niobium [23], and thermal contact resistance across the bolted connections [22,24]. Figure 21 shows the steady-state temperature profile of the cavity–thermal link assembly at 10 MeV, 100 mA accelerator operation as well as a temperature line graph along the cavity arc length from the inlet to the outlet. The simulated temperature

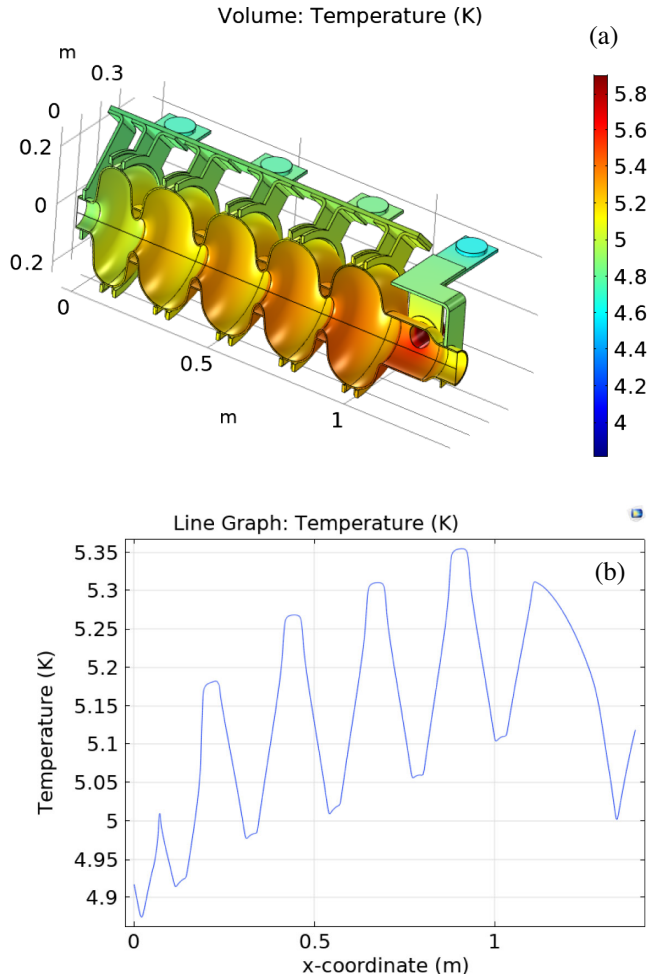

FIG. 21. Steady-state cavity temperature profile for 10 MeV, 100 mA operation (a) surface temperature map and (b) line graph along the cavity wall profile.

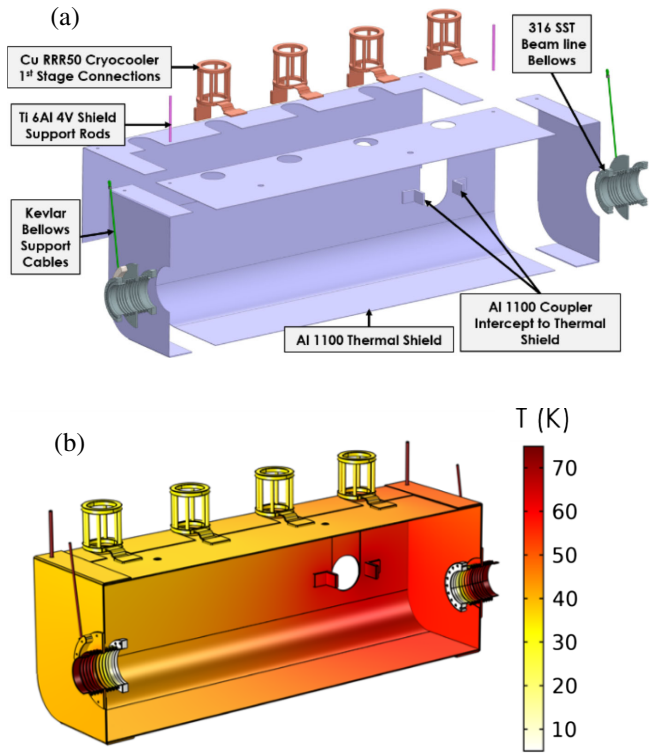

FIG. 22. (a) Thermal shield exploded view showing how the shield panels and components are assembled. (b) Thermal shield temperature distribution during steady-state operation of the accelerator.

profile shows the maximum $T_{\text{iris}} - T_{\text{equator}} < 0.25$ K and $T_{\text{cell}} - T_{\text{cryocooler}} < 0.5$ K.

The conduction cooling technique presented above has been experimentally validated by the present authors as reported in their prior work [26–28]. Therein, a single-cell 650 MHz Nb_3Sn cavity was conduction cooled using a Cryomech PT420 cryocooler. The single-cell cavity produced 10 MV/m cw accelerating gradient over a 0.23 m length. The same gradient on the present five-cell cavity is equivalent to >10 MV voltage gain.

2. Design and analysis of other cryomodule components

Thermal shield.—The thermal shield performance is evaluated using a heat transfer analysis in COMSOL Multiphysics. The COMSOL thermal model is presented in Fig. 22(a). The thermal shield, made of 2.5-mm-thick aluminum (Al1100 high thermal conductivity alloy) panels, is connected to the 50 K stages of the cryocoolers using copper thermal straps. The cryocoolers ensure the thermal shield temperature stays close to 50 K, as demonstrated below. Openings in the shield panels allow for the cryocooler heads, the support straps, the power couplers, and the beam line to be connected to the SRF cavity. In order to reduce conductive heat transfer with the surroundings, the thermal shield is suspended by a set of titanium-64 rods hanging from the top plate of the vacuum vessel.

The material thermal properties are modeled using temperature-dependent thermal conductivity data [29]. Steady-state thermal boundary conditions are imposed as follows. (i) Each rf coupler introduces 60 W of heat flux into the shield, according to the results in Table V. (ii) A thermal radiative heat flux of 1.5 W/m^2, estimated for an average thermal shield temperature of 50 K and an outer temperature of 300 K, is imposed on all outward-facing surfaces. Thermal radiation from the thermal shield at 50 K to the cavity at ~5 K is estimated to be 50 mW. Accounting for these two radiation heat flows, the net radiative heat flux incident on the thermal shield is approximately 8 W. (iii) The cavity connections to the beam line bellows are assumed at a fixed temperature of 5 K. (iv) The ambient temperature ends of the beam line bellows, titanium rods, and Kevlar support cables are set at 300 K. (v) Heat flux through the cryocooler first stages is derived empirically as $Q[W] = 117.9–3.93\ \text{T[K]}$ for PT420 cryocoolers and $Q[\text{W}] = 147.4–4.91\ \text{T[K]}$ for PT425 cryocoolers [30].

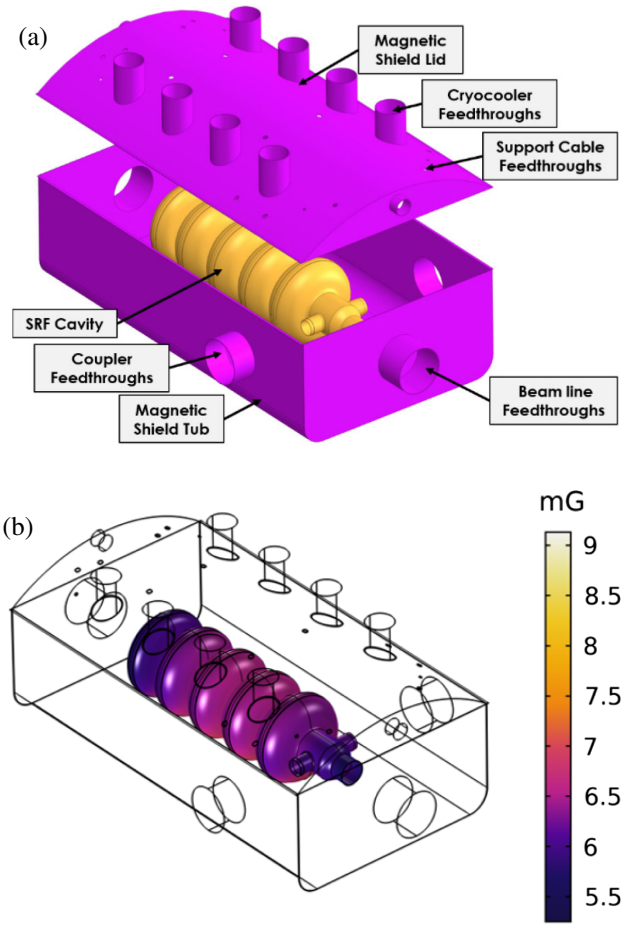

FIG. 23. (a) The exploded view of the magnetic shield shows that it is composed of two halves, a top lid, and a bottom tub which are attached at a small interface flange during assembly. Chimneys are attached around each feedthrough to improve shielding. (b) Magnetic flux density displayed along the surface of the SRF cavity, in the case where the beam line is oriented toward North.

As shown in Fig. 22(b), the thermal shield temperature varies from a minimum of 32 K at the interfaces with the cryocoolers, to 39 and 51 K at the joints with the two beam line bellows, and to a maximum of 63 K at the connections with the rf couplers. The average temperature of the thermal shield is 43 K. The cryocoolers extract a total of 137 W from the thermal shield, which is below the combined cooling capacity of the cryocoolers' 50 K stages.

Magnetic shield.—Magnetostatic simulations performed on the configuration shown in Fig. 23(a) using COMSOL Multiphysics demonstrate that a single-layer magnetic shield operating near ambient temperature between the vacuum vessel and thermal shield can adequately provide for the <10 mG target background field at the cavity surface. The simulations are performed in the local Earth magnetic field at Fermilab (Kane County, Illinois), which has a magnitude of 534 mG with components of 193, 12, and 498 mG in the North and West directions and vertically toward Earth's center, respectively [31]. The magnetic shield is modeled inside a spherical background domain of 8 m in diameter, large enough for the boundaries to not be disturbed by the presence of the magnetic shield at the center. Simulations were compared with the beam line oriented at different angles with respect to North, namely, 0°, 45°, and 90°. As shown in Fig. 23, for all three cases, the magnetic flux density along the surface of the SRF cavity is fairly uniform and does not exceed 10 mG. The peak value of the total flux at the cavity surface is 9.6 mG when the beam line is oriented at 45° with respect to North and 9 mG for the orientations at 0° and 90°. Therefore, the operation of the accelerator is expected to not be affected by its orientation with respect to North.

Vacuum vessel.—The cryomodule vacuum vessel shown in Fig. 24 is made of 316L stainless steel and consists of two parts: a bottom tub and a top lid. The lid and the tub are detachable. A vacuum seal is established using an o-ring (made of radiation resistant material such as ethylene propylene diene monomer) along the periphery, pressed using bolted connections. The vacuum vessel walls are 5/16 inch thick, and the structure is reinforced on the outside by 3/8–1/2 inch thick stiffeners that prevent buckling under external pressure. The total weight of the cryostat vacuum vessel is approximately 462 kg, i.e., 168 kg for the lid and 293 kg for the tub. Vacuum sealing features, flange bolt holes, and other small mechanical details are omitted for the evaluation of the overall structural integrity. These can be taken into account during the final design for manufacturing.

The solid mechanics module of COMSOL Multiphysics is used to evaluate stresses and buckling modes of the cryostat. Boundary conditions account for pressure differential across the vacuum vessel wall, gravity forces, the weights of the cavity, cryocoolers, rf couplers, thermal and magnetic shields, and beam line components. The material properties are assumed elastic and isotropic.

The approach of the American Society of Mechanical Engineers (ASME) Boiler and Pressure Vessel Code Sec. VIII Division 2 [32] is used to determine the structural adequacy of the vacuum vessel design. The ASME code defines the requirements for protection against three modes of failure, namely, protection against plastic collapse, protection against local failure, and protection against buckling. To avoid plastic collapse, stresses for 316L stainless steel (SA240) should remain below 16.7 ksi, according to part D, Table 5A of Ref. [32]. This criterion is verified using the maximum distortion energy yield criterion, also called von Mises criterion. The von Mises stresses are calculated at all points within the vacuum vessel and are found not to exceed the limit of 16.7 ksi; see Fig. 24(b). Regions of high stresses are located underneath the tub along the middle transversal stiffener and at the

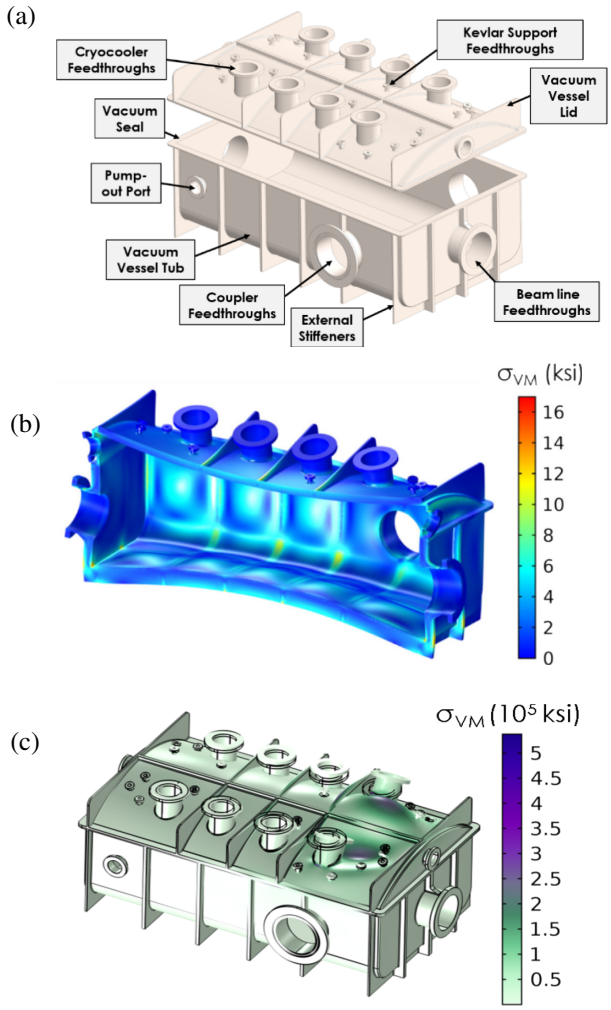

FIG. 24. (a) CAD view of the cryostat vacuum vessel made of a large tub and a lid that are sealed together. (b) Distribution of von Mises stresses due to vacuum loading (displacements exaggerated 130-fold). (c) The von Mises stresses in the vacuum vessel when the first buckling failure mode occurs on one side of the lid. The loading required for this mode of failure is approximately 64 times larger than under normal loading.

contact surfaces between the lid and the tub. The exaggerated (130 times) cryostat deformations in Fig. 24(b) indicate that the largest displacements occur at the top and bottom of the vacuum vessel but do not exceed 1 mm in amplitude. Furthermore, the risk of local failure is examined in the region of maximum von Mises stress at the bottom of the vacuum vessel. The combined membrane and bending stresses are verified to not exceed a threshold value of 25 ksi, which, according to ASME code, ensures that local failure does not occur.

To assess the risk of structural buckling when the vessel is evacuated to a vacuum, a bifurcation buckling analysis is performed using the same boundary conditions as those used for the static stress analysis above. The von Mises stresses when the first buckling mode occurs are shown in Fig. 24(c). A design safety factor, ϕ_B, is defined as the ratio

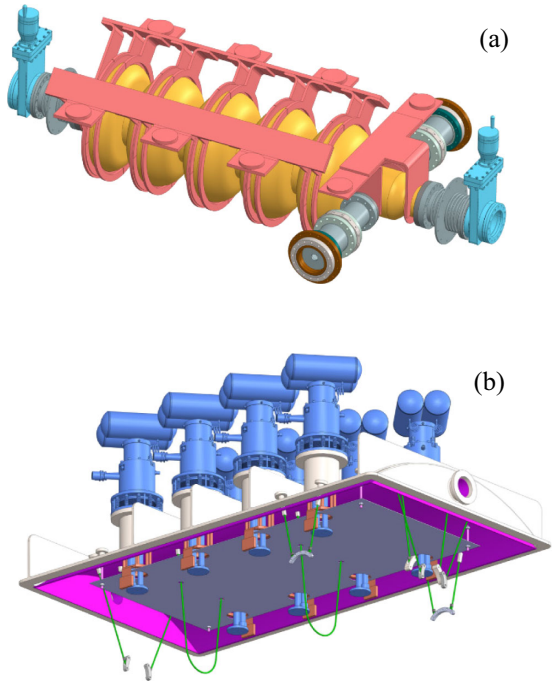

FIG. 25. CAD views of (a) the beam line assembly prior to installation in the cryocooler and (b) the beam line assembly suspended on the lid of the vacuum vessel.

of local von Mises stress when the vessel collapses by buckling to the local von Mises stress at the applied loading. The minimum allowable design safety factor is determined by $\phi_B = 2/\beta_{\text{critical}}$, where $\beta_{\text{critical}} = 0.124$ for external pressure loading. Therefore, it is required that ϕ_B remain greater than 16.1 to avoid buckling failure. The design safety factor is found to exceed 63.4 in the whole vacuum vessel, and, therefore, the vessel will not buckle when evacuated. In conclusion, the structural analysis demonstrates that the vacuum vessel well exceeds the strength requirements from ASME Sec. VIII Division 2.

F. Cryomodule assembly procedure

The cavity assembly procedure is pictorially represented in Figs. 25 and 26. Figure 25(a) shows the cavity assembly, including the thermal links, beam line bellows and valves, and vacuum side of the rf couplers, that is prepared in a clean room prior to integration with the cryomodule. This step ensures no contamination of the beam line. The top assembly of vacuum vessel, thermal shield, and magnetic shield including cryocoolers and beam line suspension components (Kevlar straps) is depicted in Fig. 25(b).

The cryomodule assembly sequence is illustrated in Fig. 26. All the shields and beam line components are suspended under the lid. To begin, all supporting cables and threaded rods are connected to the lid. The top plates of the magnetic and thermal shields, including the magnetic shield chimneys fitting in the cryocooler ports, are inserted under the lid and attached to the titanium threaded rods.

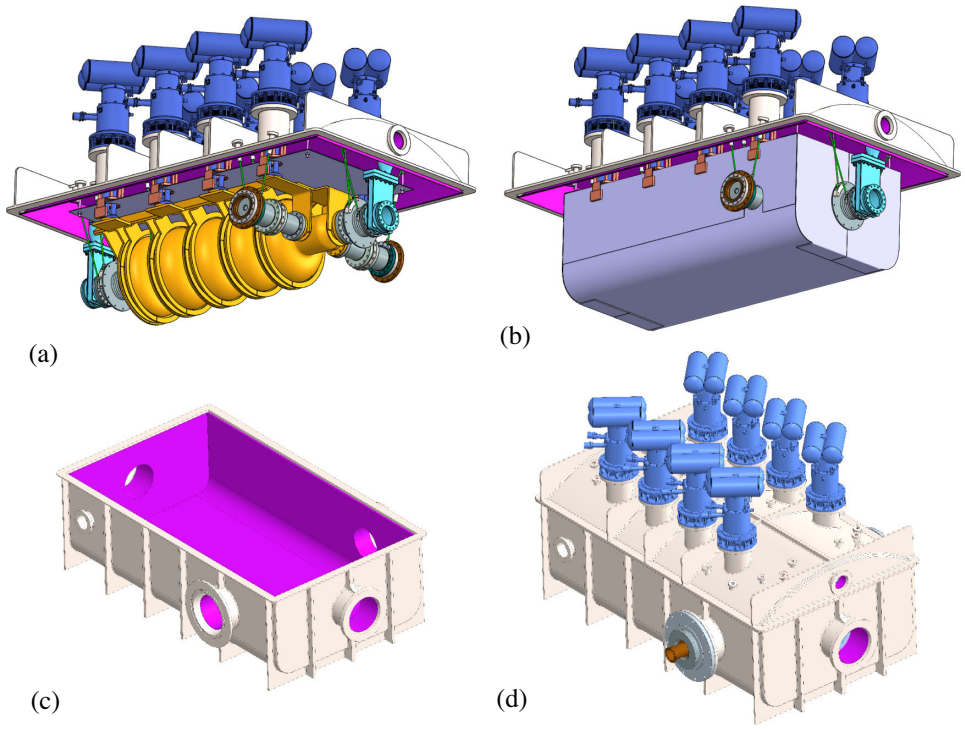

FIG. 26. Cryomodule assembly sequence. (a) Installation of the beam line assembly and cryocoolers on the vacuum vessel lid. (b) Installation of the thermal shield. (c) Installation of the bottom half of the magnetic shield inside the vacuum vessel tub and (d) fully assembled cryomodule.

Next, the evacuated cavity, with beam line bellows, gate valves, and rf couplers attached, is lifted under the lid and connected to the Kevlar straps [Fig. 26(a)]. The cryocoolers with the cylindrical thermal shield extension attached to the 50 K cooling stages are inserted through the vacuum ports and connected to the vacuum vessel using vacuum bellows. The 50 K stages of the cryocoolers are connected to the thermal shields and the 4 K cooling stages to the cavity thermal links. The next step involves assembling the rest of the thermal shield and wrapping the shield in a 30-layer multilayer insulation blanket. The rf couplers are hung from the vacuum vessel top plate using Kevlar straps [Fig. 26(b)]. The side and bottom panels of the magnetic shield are then assembled and attached inside the vacuum vessel tub [Fig. 26(c)]. Finally, the lid and all hanging components are lowered into the vacuum tub. The horizontal magnetic shield chimneys and the external flanges can be attached to the rf couplers [Fig. 26(d)]. The cryomodule is designed to be fully disassembled and put back together if needed. It has no hermetic welds.

III. ACCELERATOR WALL-PLUG EFFICIENCY AND COST ANALYSIS

A. Wall-plug-to-beam efficiency

The estimated wall-plug-to-beam efficiency of the 1 MW, 10 MeV electron beam is 41% as represented by the power flow diagram in Fig. 27. The electric power consumption is dominated by the 1 MW rf source (klystron, for instance) and the associated auxiliary systems (chillers, power supply, rf couplers, etc.), with a combined wall-plug-to-rf-power efficiency of 52%. Losses in the beam line and the beam delivery system are assumed to account for 5% of the input rf power. Additional 20 kW electrical power is required for water cooling for the eight cryocoolers. In total, 2.32 MW of total wall-plug electric power is needed to produce a 1 MW electron beam. The energy efficiency of the proposed system is comparable to the 1 MW, 1 MeV electron-beam accelerator of Ciovati *et al.* [13]. This is because the energy consumption of a megawatt-class rf linac is dominated by the rf power source. The additional cryocooling capacity required for operation of the present 10 MeV SRF cavity has a marginal impact on the overall power consumption.

B. Capital expense

The following is a detailed evaluation of the cryomodule capital expenditure (CapEx). The costs of the individual system components are provided by commercial suppliers, manufacturers, and machine shops. The CapEx of the main accelerator cryomodule is projected at approximately \$1.55 M or \$1.62 per watt of beam power. The cost breakdown per system component is presented in Fig. 28. The cost of the beam line assembly, composed of the 650 MHz Nb_3Sn cavity, the rf couplers, and

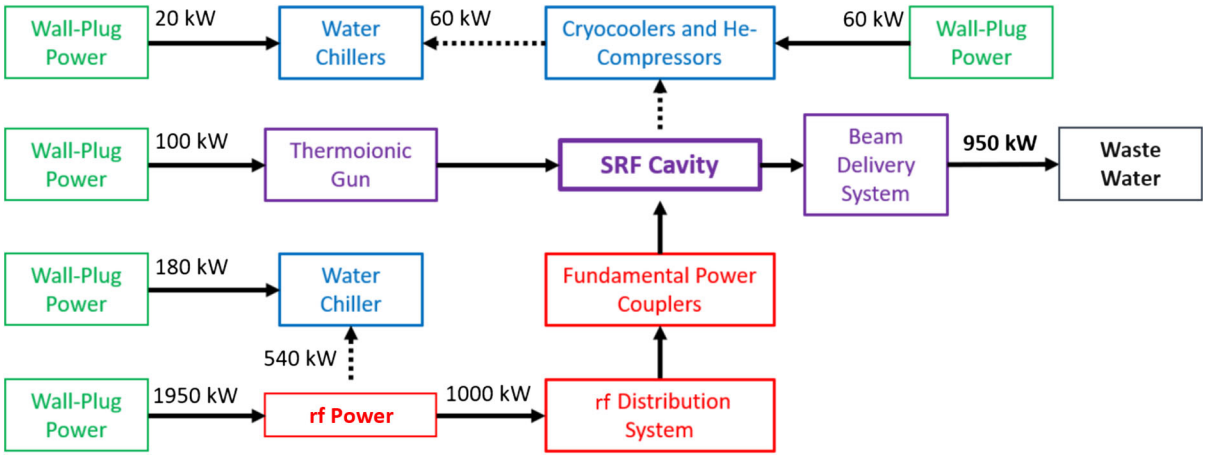

FIG. 27. Power flow diagram for the 10 MeV, 1 MW SRF accelerator.

additional beam line components (valves, bellows, and HOM absorber), represents ~50% of the cryomodule CapEx. The eight cryocoolers and the individual helium compressors sum up to approximately \$500 k, which is 32% of the cryomodule CapEx. The cost of fabrication of the vacuum vessel and the thermal and magnetic shields is \$181 k, which represents 12% of the cryomodule CapEx. The cost of labor associated with the installation of the beam line and the assembly of the cryomodule is not accounted for in Fig. 28.

The CapEx of the 1 MW, 1 MeV SRF linac, including the rf source (klystron), the electron gun, the beam delivery system, and the beam diagnostics, was estimated to be \$4.5 M by Ciovati *et al.* [13]. Based on Ciovati *et al.*'s costing, the CapEx of the present *e*-beam accelerator is projected to be \$5.1 M. Table VIII presents a component-wise breakdown of the accelerator CapEx. Ciovati *et al.*'s 1 MeV linac and the present 10 MeV linac are thought to mostly differ in the design of the cryomodule, the remaining systems being similar or identical. The 10 MeV cryomodule in this study is 67% more expensive than the 1 MeV cryomodule of Ciovati *et al.* The rf power source remains the largest expenditure in the accelerator CapEx. Ciovati *et al.* also evaluated the cost of a 1 MW klystron and all auxiliary systems (power supplies, controllers, rf power distribution, water chillers, etc.) to \$3.2 M, which exceeds the cost of the 10 MeV cryomodule by a factor of 2. Alternatives to klystrons such as multibeam inductive output tubes and solid-state rf drivers do not offer any substantial economic or performance benefits at this time. Significant developments in megawatt-class UHF cw rf source technologies are needed to lower the capital cost and increase the rf efficiency. Megawatt-class rf power sources based on the combined power of multiple low-cost cw magnetrons are in development [33].

The labor cost of accelerator assembly is excluded at the present design stage from capital cost, because a reasonable number can be determined only via a prototype construction and assembly exercise. The labor estimate will also depend on which organization does the assembly, i.e., a national lab, a private accelerator company, or a manufacturing contractor,

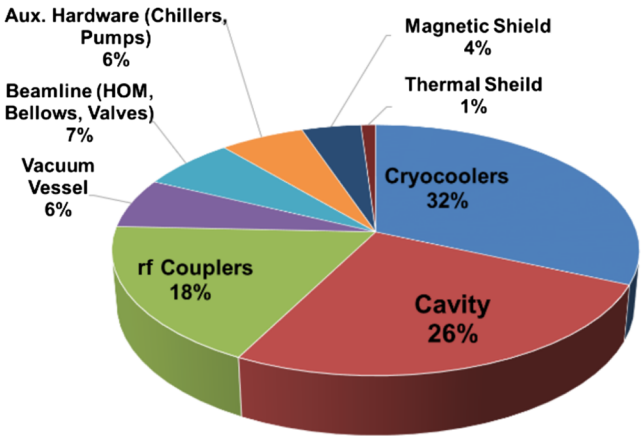

FIG. 28. Cost breakdown of the SRF cryomodule assembly.

TABLE VIII. Capital cost of the 1 MW, 10 MeV SRF accelerator.

Item	Cost [*k*\$]
1 MW rf power source [13]	3200
Electron injector [13]	217
Beam delivery system [13]	125
Beam diagnostics and controls [13]	38
SRF cryomodule	1554
Cryocoolers with He compressors	492
650 MHz Nb_3Sn cavity	402
rf couplers	282
Vacuum vessel	100
Beam line (bellows, valves)	104
Auxiliary hardware (chillers, pumps)	93
Magnetic shield	65
Thermal shield	16
Total	5134

etc., which have very different labor rates as well as overheads.

While still in infancy, the SRF linac designed in the present work has the potential to reduce the cost of industrial megawatt-class SRF accelerators. Here, we compare the capital cost ($5.1 M) of the present 10 MeV, 1000 kW SRF linac with similar machines available commercially [34]. The Budker Institute of Nuclear Physics ILU-14 rf linac delivering 10 MeV, 100 kW electron beam carries a price tag of $5.1 M, which means that a capital cost of >$50 M will be required to obtain 1000 kW beam power. An ion beam applications Rhodotron rf-SCR machine costs $8 M for a 7 MeV, 560 kW electron beam. The present SRF linac exceeds in beam energy and average power and is still expected to be cheaper than the ion beam applications Rhodotron.

C. Infrastructure and accelerator operating expense

The operating expense (OpEx) of the proposed accelerator, detailed in Table IX, is extrapolated from the costing analysis of Ciovati *et al.* [13] and estimated at $278 per hour of operation. The cost of infrastructure installation (radiation shielding, material delivery system, etc.) is accounted separately from the accelerator CapEx. Ciovati *et al.* estimated the total cost of infrastructure to $2.75 M. The present *e*-beam accelerator necessitates additional shielding than at 1 MeV. The absorbed doses in the forward direction for 1 and 10 MeV electron beams are approximately 2.75×10^{-3} rads* m^2/(hr* kW) and 3.00×10^{-5} rads* m^2/(hr* kW), respectively [35]. Therefore, operation of a 10 MeV linac is anticipated to require approximately 20% more shielding (e.g., concrete wall thickness) than for a 1 MeV accelerator of equivalent beam power. As a result, the cost of infrastructure for the present linac is projected to be $3.0 M. The total cost of fabrication and installation of the *e*-beam facility is therefore estimated to be $8.1 M. Calculations with a 20% loan investment with 15-year amortization are listed in Table IX.

Similar to Ciovati *et al.*, the operating cost is derived under the assumption of high usage of the linac to 8000 hours per year. The remaining down time is allocated to maintenance operations. The average annual cost of maintenance is estimated at 2% of the capital cost of the linac facility, which results in an estimated annual maintenance budget of $163 k. The cost of electric power consumption is based on an electricity rate of $0.07 per kWh, which results in $162 per hour of operation. The linac systems are designed with closed loop water systems and air-cooled chillers. As a result, water consumption is considered negligible. The industrial linac is envisioned as a turn-key system requiring minimal supervision and no specialized or dedicated personnel. Therefore, labor is not accounted for in the operating cost.

TABLE IX. Capital investment and estimated cost of operating the 1 MW, 10 MeV SRF accelerator.

Item	Cost
SRF accelerator	$5.13 M
Infrastructure	$3 M
Investment (20%)	$1.63 M
Amortization (15 yrs @ 8%)	$760 per year
Operating cost	$278 per hr
Power ($/W)	$162 per hr
Maintenance	$163 k per year
Material processing cost	13.5 ¢/ton/kGy

D. Wastewater processing cost

The wastewater processing cost is defined in units of ¢/ton/kGy and represents the cost of a unit dose of 1 kGy deposited in 1 ton of the material. The processing cost of the present linac is estimated at 13.5 ¢/ton/kGy, which is only 6% higher than for the linac of Ciovati *et al.* [13] even though our energy is 10 times higher and, thus, can penetrate higher depth (~45 mm at 10 MeV compared to ~5 mm at 1 MeV). This larger penetration depth can enable handling an approximately tenfold larger interaction volume, which could be important in large-city-scale water treatment facilities. This analysis demonstrates that a 10 MeV SRF linac is not excessively more expensive than a 1 MeV system of the same power capacity. For wastewater treatment where a dosage of 1–4 kGy may be required, the present system could offer a processing capacity of 3–12 MGD for a cost of $500–$2000 per megagallon of water. For applications requiring a significant higher dosage such as 50 kGy for medical waste sterilization, the present linac has the potential to process 48 tons of waste materials per hour at a cost of 5.8 per ton.

IV. SUMMARY AND OUTLOOK

We presented detailed beam dynamics, rf, thermal, and engineering design of a 10 MeV, 1 MW average power *e*-beam accelerator driven by a room-temperature preaccelerator and a conduction-cooled SRF accelerator cryomodule. The technical design is supplemented by a detailed analysis of capital or construction and operation cost of the *e*-beam accelerator. The analysis determined that the capital cost is around $8 per watt of beam power, while 13.5 ¢/ton/kGy is required for irradiation processing. We consider the accelerator of size 4 m × 2 m × 2 m to be a compact one that can be conveniently set up at municipal and industrial wastewater treatment facilities. While one accelerator unit can treat up to 12 MGD of wastewater, the installation can be easily scaled up for higher volumes by deploying multiple accelerator units.

While the simulation-based design produced in this work appears to be technically feasible as well as cost appealing, a few areas need further practical development. These

include production of high-Q_0 multicell Nb_3Sn cavities, continued research on conduction cooling techniques that better thermalize the cavity with the cryocoolers, probing and suppressing microphonics that can result from cryocooler vibration, and more. As noted in Fig. 27, the rf power source is the dominant consumer of electrical power required to drive the *e*-beam accelerator. Further research and development on rf sources of potentially higher wall-plug-to-rf efficiency should be undertaken for lowering the overall accelerator operating cost. Since the rf power source is also expected to be the major capital cost driver (Table VIII), it is also essential to explore lower-cost alternatives for manufacturing the power sources. Therefore, a low-cost high-efficiency rf power source development is key to fully exploiting the SRF accelerator technology for environmental applications.

ACKNOWLEDGMENTS

This manuscript has been authored by Fermi Research Alliance, LLC under Contract No. DE-AC02-07CH11359 with the U.S. Department of Energy, Office of Science, Office of High Energy Physics. Research funded by an Accelerator Stewardship grant to Fermilab by U.S. Department of Energy, Office of Science, Office of High Energy Physics.

[1] R. Schoenlein, T. Elsaesser, K. Holldack, Z. Huang, H. Kapteyn, M. Murnane, and M. Woerner, Recent advances in ultrafast x-ray sources, Phil. Trans. R. Soc. A **377**, 20180384 (2019).

[2] W. Henning and C. Shank, Accelerators for America's future, available online at https://science.osti.gov/-/media/hep/pdf/files/pdfs/Accel_for_Americas_Future_final_report.pdf, 2010.

[3] M. Jenkins, G. Burt, and A. V. Praveen Kumar, Prototype 1 MeV X-band linac for aviation cargo inspection, Phys. Rev. Accel. Beams **22**, 020101 (2019).

[4] R. Kostin, C. Jing, P. Avrakhov, Y. Zhao, and A. Liu, Status of conduction cooled SRF photogun for UED/UEM, in *Proceedings of the 12th International Particle Accelerator Conference (IPAC2021), Campinas, SP, Brazil* (Joint Accelerator Conferences, 2021), p. 1773, 10.18429/JACoW-IPAC2021-TUPAB167.

[5] IAEA, Radiation Technology for Cleaner Products and Processes, Report No. IAEA-TECDOC-1786, 2016.

[6] A. G. Chmielewski, Electron accelerators for environmental protection, Rev. Accel. Sci. Techol. **04**, 147 (2011).

[7] T. D. Waite, C. N. Kurucz, W. J. Cooper, and D. Brown, Full scale electron beam systems for treatment of water, wastewater and medical waste, in *Proceedings of the Symposium on Radiation Technology for Conservation of the Environment, Zakopane, Poland* (International Atomic Energy Agency, Vienna, 1998), p. 187, https://inis.iaea.org/search/search.aspx?orig_q=RN:29050419.

[8] B. Han, J. K. Kim, Y. Kim, J. S. Choi, and K. Y. Jeong, Operation of industrial-scale electron beam wastewater treatment plant, Radiat. Phys. Chem. **81**, 1475 (2012).

[9] S. He, W. Sun, J. Wang, L. Chen, Y. Zhang, and Y. Jiang, Enhancement of biodegradability of real textile and dyeing wastewater by electron beam irradiation, Radiat. Phys. Chem. **124**, 203 (2016).

[10] IAEA, China's Electron Beam Industry Opens World's Largest Wastewater Treatment Facility, available online at https://www.iaea.org/newscenter/news/started-with-iaea-support-chinas-electron-beam-industry-opens-worlds-largest-wastewater-treatment-facility, 2021.

[11] J. C. T. Thangaraj, A. Saini, V. Yakovlev, I. Gonin, N. Solyak, R. C. Dhuley, T. Kroc, M. Geelhoed, I. Tropin, N. Mokhov, and T. Khabiboulline, Conceptual design of a 10-megawatt electron beam irradiation facility for bio-solid waste treatment, 2018, report, available online at 10.2172/1638675.

[12] G. Ciovati, ac/rf superconductivity, arXiv:1501.07398v1.

[13] G. Ciovati, J. Anderson, B. Coriton, J. Guo, F. Hannon, L. Holland, M. LeSher, F. Marhauser, J. Rathke, R. Rimmer, T. Schultheiss, and V. Vylet, Design of a cw, low-energy, high-power superconducting linac for environmental applications, Phys. Rev. Accel. Beams **21**, 091601 (2018).

[14] R. Nagimov, I. Bylinsky, D. Kishi, S. Koscielniak, A. Koveshnikov, R. Laxdal, and D. Yosifov, The operational experience of e-linac cryogenic system at TRIUMF, in *Proceedings title: Proceedings of the 9th International Particle Accelerator Conference (IPAC2018), Vancouver BC, Canada* (Joint Accelerator Conferences, 2018), p. 3928, 10.18429/JACoW-IPAC2018-THPAL121.

[15] R. C. Dhuley and S. W. V. Sciver, Propagation of nitrogen gas in a liquid helium cooled vacuum tube following sudden vacuum loss—Part I: Experimental investigations and analytical modeling, Int. J. Heat Mass Transfer **96**, 573 (2016).

[16] R. C. Dhuley and S. W. V. Sciver, Propagation of nitrogen gas in a liquid helium cooled vacuum tube following sudden vacuum loss—Part II: Analysis of the propagation speed, Int. J. Heat Mass Transfer **98**, 728 (2016).

[17] J. Petillo, K. Eppley, D. Panagos, P. Blanchard, W. Krueger, A. Mondelli, T. McClure, B. Levush, J. Burdette, M. Cattelino, J. DeFord, B. Held, N. Dionne, S. Humphries, Jr., E. Nelson, and R. True, The MICHELLE electron gun and collector modeling tool, in *Proceedings of the 19th Particle Accelerator Conference, Chicago, IL, 2001* (IEEE, Piscataway, NJ, 2001), p. 3054.

[18] O. Pronitchev and S. Kazakov, Design of main coupler for 650 MHz SC cavities of PIP-II project, in *Proceedings title: Proceedings of 2nd North American Particle Accelerator Conference (NAPAC2016), Chicago IL, USA* (Joint Accelerator Conferences, 2016), p. 121, 10.18429/JACoW-NAPAC2016-MOPOB24.

[19] R. C. Dhuley, M. Ruschman, J. T. Link, and J. Eyre, Thermal conductance characterization of a pressed copper rope strap between 0.13 K and 10 K, Cryogenics **86**, 17 (2017).

[20] W. Xu, Z. Altinbas, S. Belomestnykh, I. Ben-Zvi, M. Cole, S. Deonarine, M. Falletta, J. Jamilkowski, D. Gassner, P. Kankiya, D. Kayran, N. Laloudakis, L. Masi, Jr.,

G. McIntyre, D. Pate, D. Philips, T. Seda, T. Schultheiss, A. Steszyn, T. Tallerico, R. Todd, D. Weiss, G. Whitbeck, and A. Zaltsman, Design, simulations, and conditioning of 500 kW fundamental power couplers for a superconducting rf gun, Phys. Rev. Accel. Beams **15**, 072001 (2012).

[21] SRIMP, available online at https://www.classe.cornell.edu/~liepe/webpage/researchsrimp.html.

[22] R. Dhuley, R. Kostin, O. Prokofiev, M. Geelhoed, T. H. Nicol, S. Posen, J. Thangaraj, T. Kroc, and R. Kephart, Thermal link design for conduction cooling of SRF cavities using cryocoolers, IEEE Trans. Appl. Supercond. **29**, 0500205 (2019).

[23] F. Koechlin and B. Bonin, Parametrization of the niobium thermal conductivity in the superconducting state, Supercond. Sci. Technol. **9**, 453 (1996).

[24] R. C. Dhuley, M. I. Geelhoed, and J. C. T. Thangaraj, Thermal resistance of pressed contacts of aluminum and niobium at liquid helium temperatures, Cryogenics **93**, 86 (2018).

[25] A. Saini, V. Lebedev, N. Solyak, and V. Yakovlev, Estimation of cryogenic heat loads in cryomodule due to thermal radiation, in *Proceedings of 6th International Particle Accelerator Conference (IPAC2015), Richmond VA, USA* (Joint Accelerator Conferences, 2015), p. 3338, 10.18429/JACoW-IPAC2015-WEPTY031.

[26] R. C. Dhuley, S. Posen, M. I. Geelhoed, O. Prokofiev, and J. C. T. Thangaraj, First demonstration of a cryocooler conduction cooled superconducting radiofrequency cavity operating at practical cw accelerating gradients, Supercond. Sci. Technol. **33**, 06LT01 (2020).

[27] R. C. Dhuley, M. I. Geelhoed, Y. Zhao, I. Terechkine, M. Alvarez, O. Prokofiev, and J. C. T. Thangaraj, Demonstration of CW accelerating gradients on a cryogen-free, cryocooler conduction-cooled SRF cavity, IOP Conf. Ser. Mater. Sci. Eng. **755**, 012136 (2020).

[28] R. C. Dhuley, S. Posen, M. I. Geelhoed, and J. C. T. Thangaraj, Development of a cryocooler conduction-cooled 650 MHz SRF cavity operating at ∼10 MV/m cw accelerating gradient, arXiv:2108.09397.

[29] NIST, Cryogenic material properties database, available online at https://trc.nist.gov/cryogenics/materials/materialproperties.htm.

[30] Cryomech, Data on pulse tube cryocoolers, available online at https://www.cryomech.com/cryocoolers/pulse-tube-cryocoolers/.

[31] IAGA V-MOD, Local magnetic field at Fermilab site, referenced from https://www.ngdc.noaa.gov/IAGA/vmod/igrf.html.

[32] D. A. Osage, C. D. Rodery, T. P. Pastor, R. G. Brown, P. A. Henry, and J. Sowinski, ASME Section VIII: Division 2-alternative rules, in *Companion Guide to the ASME Boiler and Pressure Vessel Code*, Vol. 2, edited by K. R. Rao (ASME, New York, 2012).

[33] X. Chen, B. Yang, N. Shinohara, and C. Liu, A high-efficiency microwave power combining system based on frequency-tuning injection-locked magnetrons, IEEE Trans. Electron Devices **67**, 4447 (2020).

[34] 2015 DOE Workshop on Energy and Environmental Applications of Accelerators, available online at https://science.osti.gov/hep/Research/Accelerator-Stewardship/Workshop-Reports.

[35] National Council on Radiation Protection and Measurements, Radiation protection for particle accelerator facilities, NCRP Report No. 144, 2003.